Supporting Information: Evaluating size effects on the thermal conductivity and electron-phonon scattering rates of copper thin films for experimental validation of Matthiessen's rule

Md. Rafiqul Islam[1], Pravin Karna[2], John A. Tomko[3], Eric R. Hoglund[3], Daniel M. Hirt[1], Md Shafkat Bin Hoque[1],Saman Zare [1], Kiumars Aryana[1], Thomas W. Pfeifer[1], Christopher Jezewski[4], Ashutosh Giri[2], Colin D. Landon[5], Sean W. King[6], and Patrick E. Hopkins[1,3,7,*]

[1]Department of Mechanical and Aerospace Engineering, University of Virginia, Charlottesville, Virginia 22904, USA

[2]Department of Mechanical Industrial and Systems Engineering, University of Rhode Island,Kingston, RI 02881, USA

[3]Department of Materials Science and Engineering, University of Virginia, Charlottesville,Virginia 22904, USA

[4]Components Research, Intel Corporation, Hillsboro, Oregon 97124, USA

[5]Logic Technology Development, Intel Corporation, Hillsboro, Oregon 97124, USA

[6]Supplier, Technology, and Industry Development, Intel Corporation, Hillsboro, Oregon 97124, USA

[7]Department of Physics, University of Virginia, Charlottesville, Virginia 22904, USA

Contents

S1. Scanning transmission electron microscopy (STEM) characterization of Cu films

A series of Cu films ranging from 27 nm to 5 µm thick were grown on 3nm Ta/100 nm SiO_2/Si (001) 300 mm diameter wafers at temperatures < 30 °C using industry standard physical vapor deposition (PVD) and electroplating (EP) tools and method [1,2]. We encounter practical constraints when attempting to grow Cu films through PVD beyond a thickness of approximately 100 nm. Consequently, we opt to synthesize films exclusively at thicknesses of 27, 57, and 118 nm using the PVD technique. To produce thicker films exceeding 100 nm, we resort to EP methods, supplemented by a 10 nm fixed PVD Cu seed layer, abbreviated as PVD-EP. To vary the microstructure of the Cu films, we anneal a sub-set of these as-deposited films at 300 °C, 400 °C and 500 °C for 15 minutes in argon.

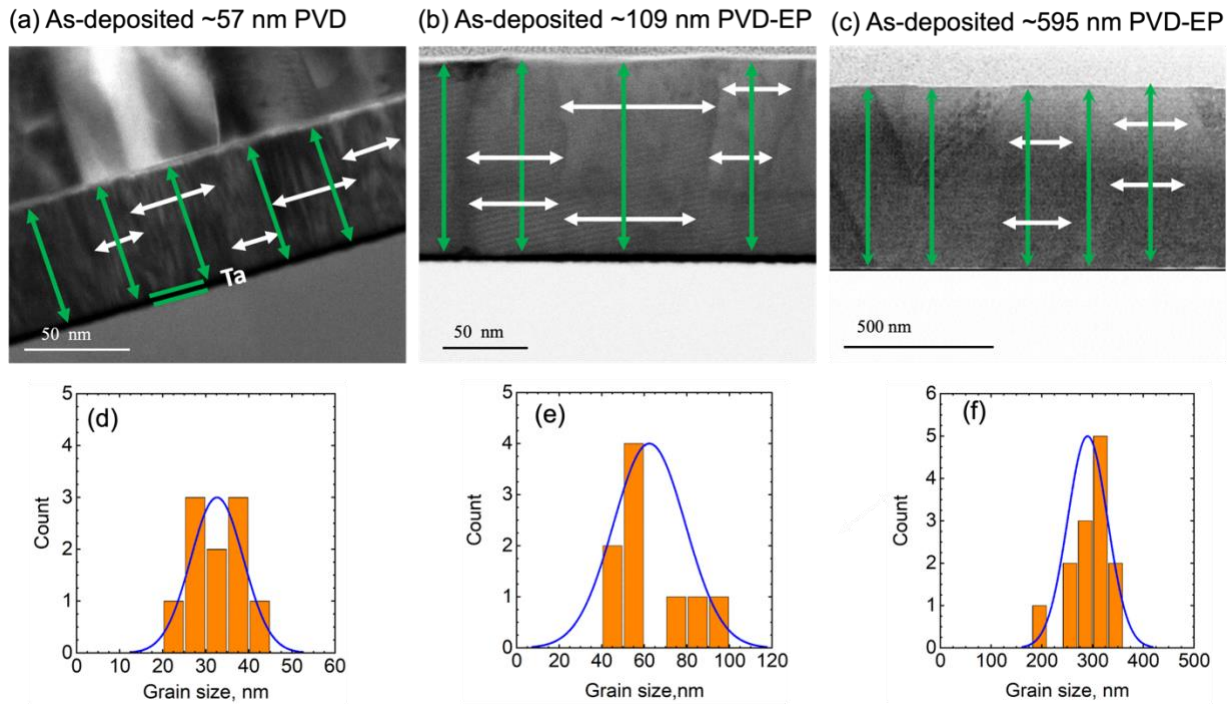

Figure S1: TEM image for (a) ~57 nm PVD and STEM micrographs for (b) ~109 nm and (c) ~595 nm PVD-EP grown as-deposited Cu films. The green arrows indicate the thickness. (d), (e) and (f) represent the grain size distribution of ~57 nm PVD, ~109 nm and ~595nm PVD-EP films respectively

We examine the grain morphology and chemical composition of the as-deposited and annealed PVD and PVD-EP Cu films by scanning transmission electron microscopy (STEM). The thickness and grain size of the films are determined over a large area. In Figure S1, we show the representative area of the as-deposited films. We find that the thickness of PVD films is uniform, however, PVD-EP films exhibit non-uniform thickness across a significant area as listed in Table 1(main manuscript). There was no noticeable porosity in the films. The grains of these films are columnar as shown in Figure S1. The size of the grains is listed in Table 1 (main manuscript). The grain size increases with film thickness. The grain size does not vary significantly for as-deposited PVD and PVD-EP films with comparable thicknesses. Furthermore, the 118 nm PVD and 109

PVD-EP films are textured and 118 nm PVD films consist of twin regions with twin boundaries arranged along [111] axis. Figure S2 shows SAED image with a diffraction contrast appearing at the twin plane [111]. The PVD grown 118 nm film contains more twinning than the 109 nm PVD-EP film. The grain size smaller than the electron mean free path reduces the in-plane thermal conductivity as shown in Figure S28.

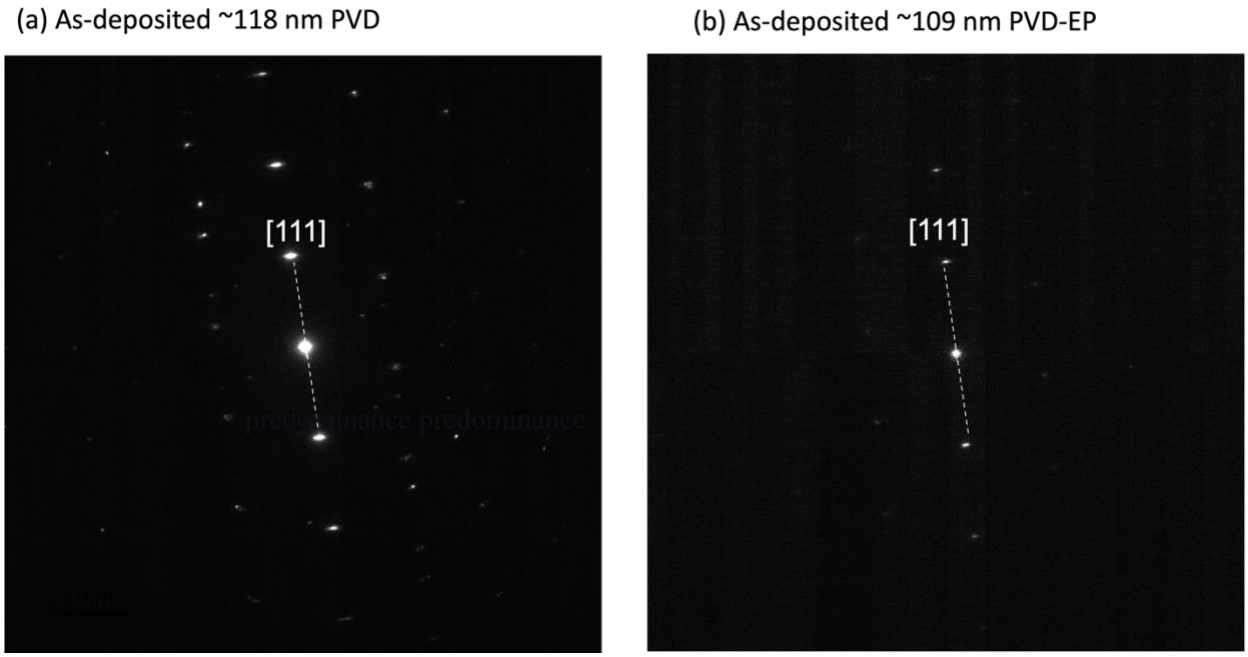

Figure S2– The selected area electron diffraction pattern of the 118 nm PVD and 109 PVD-EP films obtained using TEM. Both films are textured and 118 nm films consist of twin regions with twin boundaries arranged along [111] axis

We also study the effect of annealing on the grain size of Cu films. Figure S3 shows the morphology and grain size of the annealed PVD and PVD-EP films at 500 °C. We find an increase in their grain size as listed in Table 1 (main manuscript).

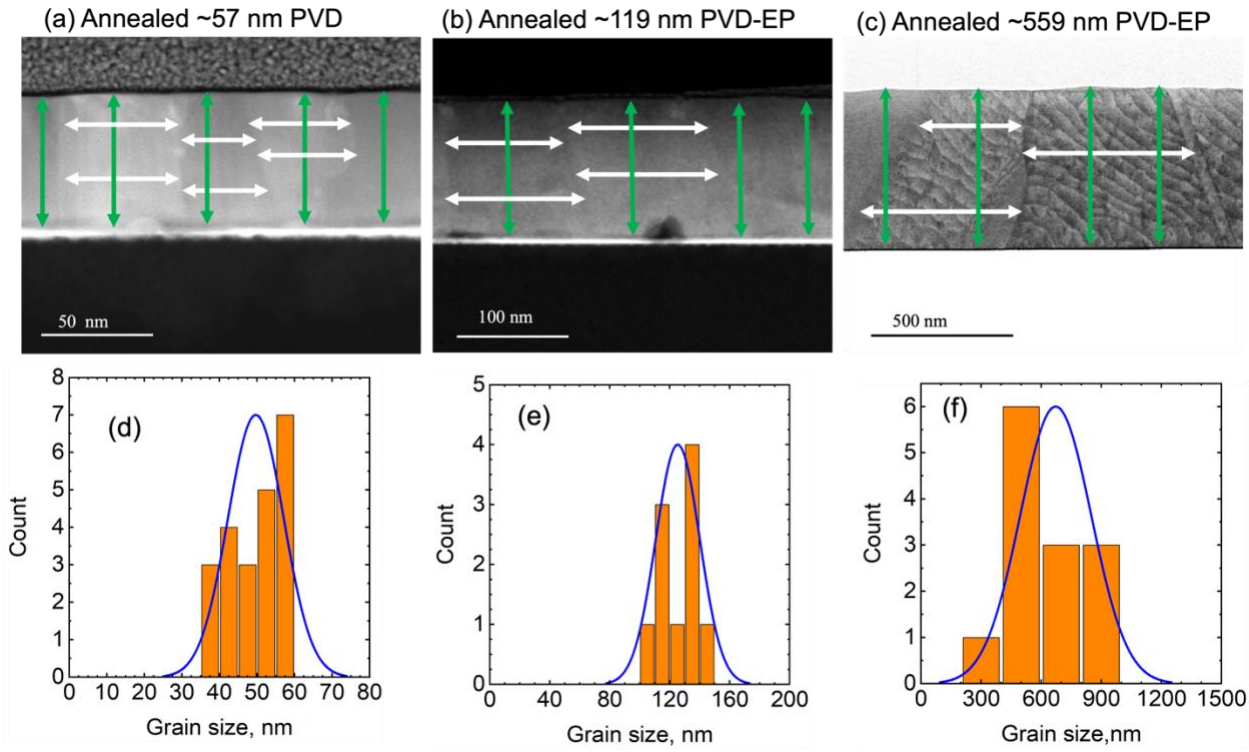

Figure S3: STEM micrographs for (a)~ 57 nm PVD, (b) ~119 nm PVD-EP and (c) ~559 nm PVD-EP method grown annealed Cu films at 500 ℃. The green arrows indicate the thickness. (d), (e) and (f) represent the grain size distribution of ~57 nm PVD, ~119 nm and ~559nm PVD-EP films respectively. The grain size of the ~119 nm and ~559 nm Cu films increases due to annealing at 500 ℃

The Cu films may contain nitrogen (N), chlorine (Cl) or sulfur (S) from the platter, super fill chemistry, brightener, leveler, etc. The EDX spectrum of PVD and PVD-EP films indicates that they do not contain these impurities. Figure S4 shows that there are oxygen and silicon in the EDX signal of the as-deposited 27 and 118 nm PVD films which comes from the underneath 100 nm SiO_2 layer. The atomic fraction of oxygen and silicon match the stoichiometry of O and Si in SiO_2. However, the films grown with as-deposited PVD-EP films seem to contain oxygen (atomic fraction =1.88-3.61%) as copper oxide (Figure S5 and Table S1). This oxygen could be introduced during transferring prepared thin samples from FIB to the chamber of TEM. We also cannot ignore this source of oxygen could be from 1-2 nm native copper oxide formed on the Cu surface. The atomic fraction of oxygen and silicon is listed in Table S1. The in-plane thermal conductivity and electrical thermal conductivity of 118nm PVD and 109 nm PVD-EP films are found to be the same. Therefore, this amount of oxygen is not considerable to impact the in-plane thermal conductivity and electron-phonon scattering rates at room temperatures implying that our size-dependent thermal conductivity and electron-phonon scattering rates study is independent of synthesis method. We also find the presence of carbon (C) and molybdenum (Mo) in EDX spectrum. This is attributed to the fact that we deposit carbon on Cu films to obtain a clean surface which makes it easy to identify the top of the surface layer under FIB-SEM and TEM. The Mo peak visible in the EDX spectrum appears as spurious signal due to the presence of the Mo grid. We also find Ti signal in EDX spectrum of 27 nm PVD film because this EDX characterization

was performed on Al/Ti/ coated 27 nm Cu film. In summary, EDX analysis proves that our as-deposited Cu films are free of general impurities, but the films grown using PVD-EP films contains a small amount of oxygen.

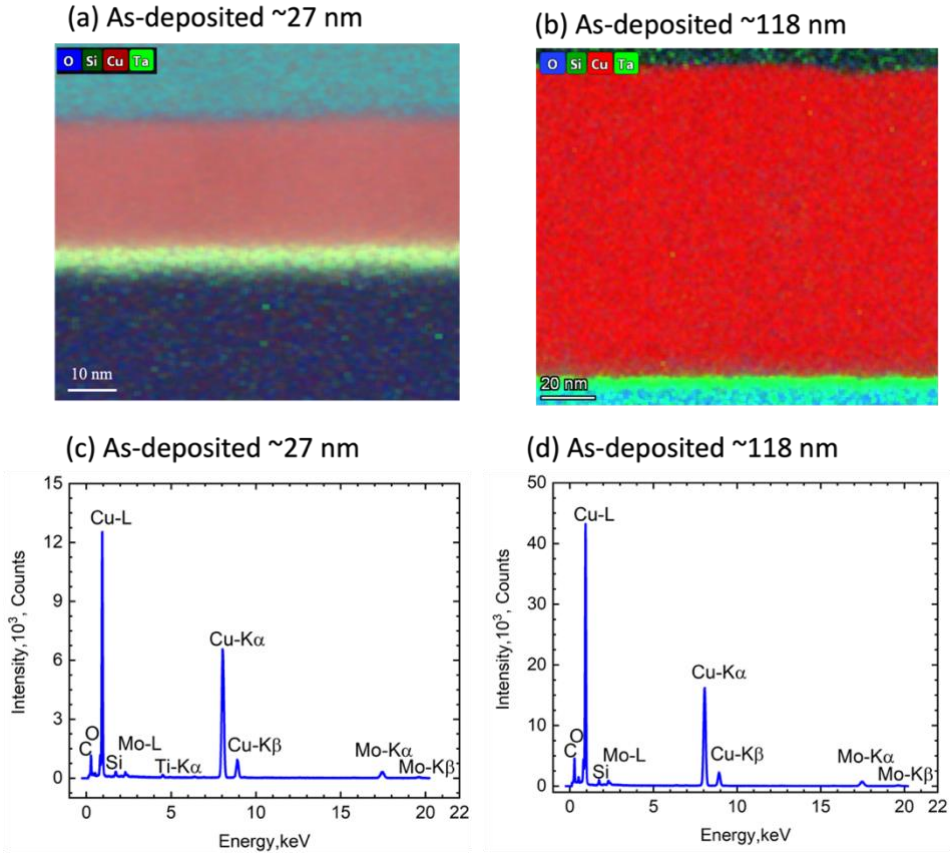

Figure S4: STEM- EDX mapping and spectrum of as-deposited 27 and 118 nm PVD films.

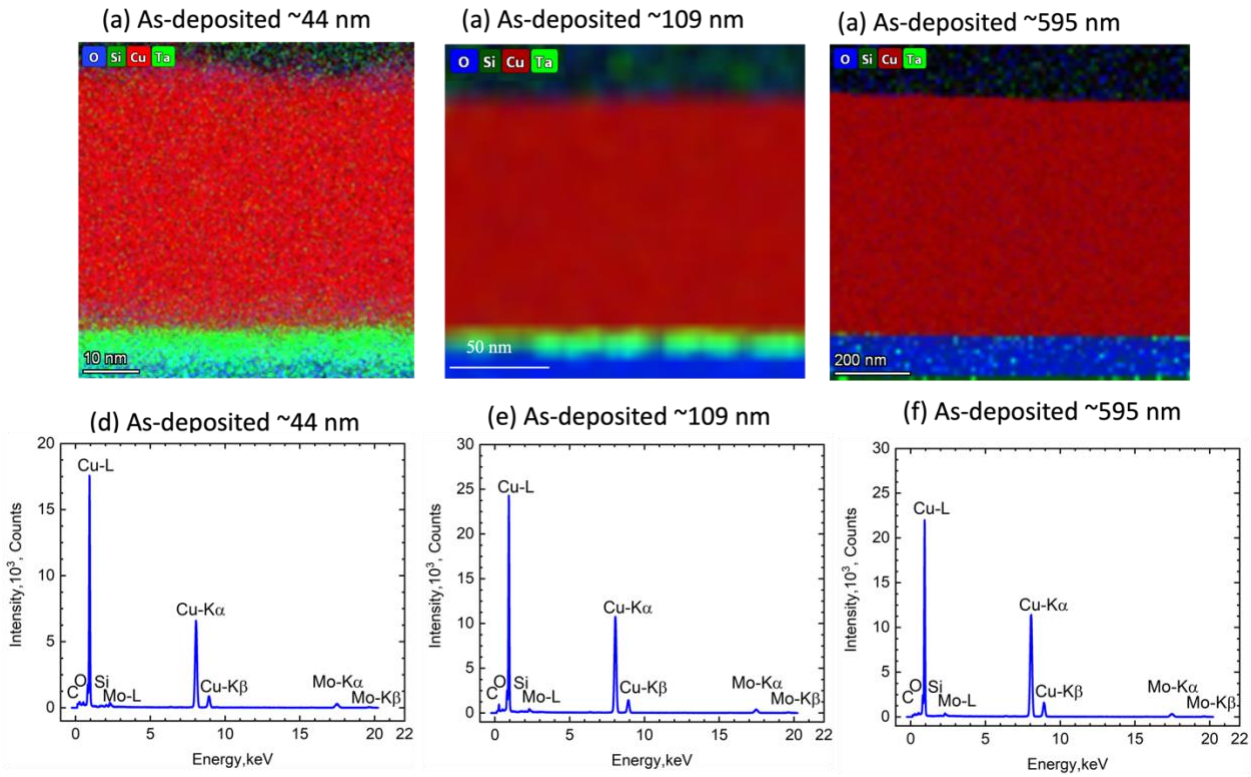

Figure S5: STEM- EDX mapping and spectrum of as-deposited 44, 109 and 595 nm PVD-EP films.

Table S1: The atomic fraction of oxygen and silicon from EDX analysis on as-deposited Cu films

PVD films, nm	Oxygen atomic fraction (%)	Silicon atomic fraction (%)	PVD-EP films nm	Oxygen atomic fraction (%)	Silicon atomic fraction (%)
27	1.9±0.01	1.1±0.01	44	3.6±0.11	0.03±0.002
118	7.8±0.14	3.8±0.04	109	1.9±0.05	0.60±0.03
			595	1.9±0.05	0.006±0.0012

We also determine the composition of the annealed films using EDX. There is a noticeable TaO_x complexes formation along the grain boundaries of annealed 27 nm PVD film as shown in the Figure S6. However, there is no TaO_x formation for annealed 57 nm and 119 nm PVD films as shown in Figure S6 (b and c). We find a negligible amount of Ta (atomic fraction=0.08 %) in annealed PVD-EP Cu film as listed in Table S2. However, thicker PVD-EP films are free from Ta

diffusion as shown in Figure S7 and Table S2. Like as-deposited film the EDX spectrum of both annealed PVD and PVD-EP films contain oxygen and silicon. As aforementioned for as-deposited films, this oxygen signal is coming from underlayer SiO_2 or formation of oxide after the sample preparation by FIB technique or due to surface native copper oxide.

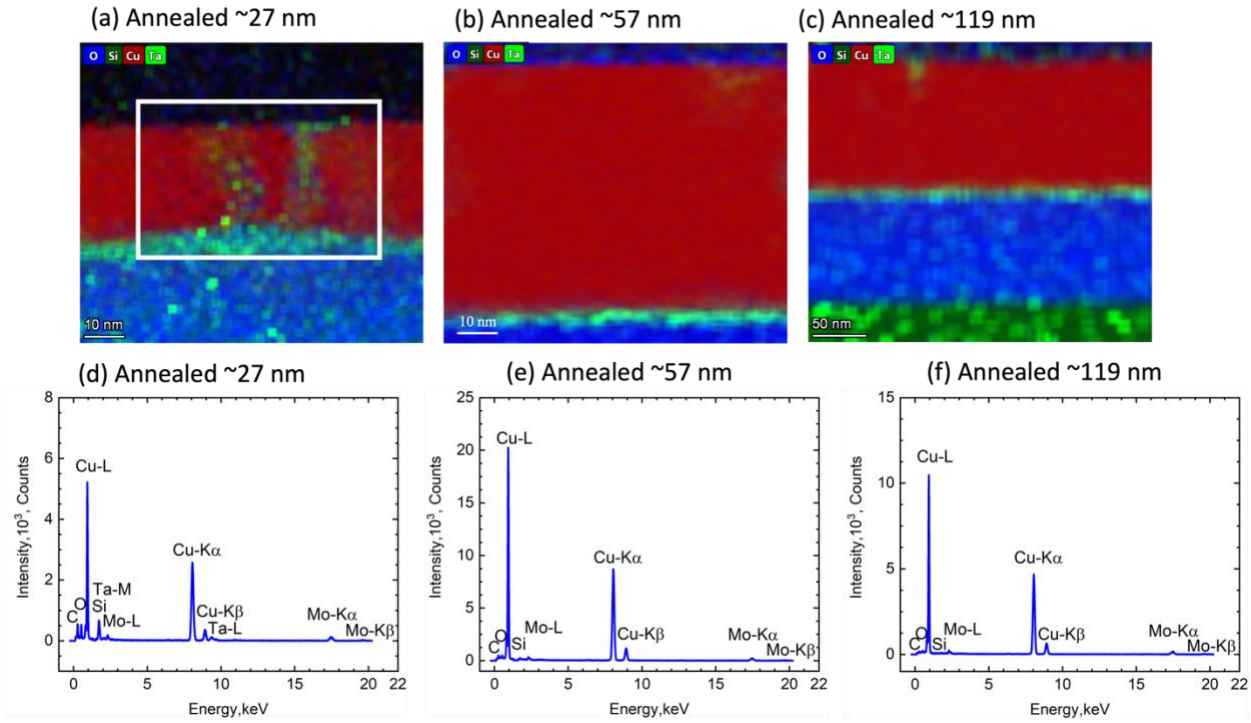

Figure S6: STEM- EDX mapping and spectrum of annealed 27,57 and 119 nm PVD films. The presence of carbon (C) and molybdenum (Mo) in EDX spectrum is related to FIB-SEM and TEM characterization.

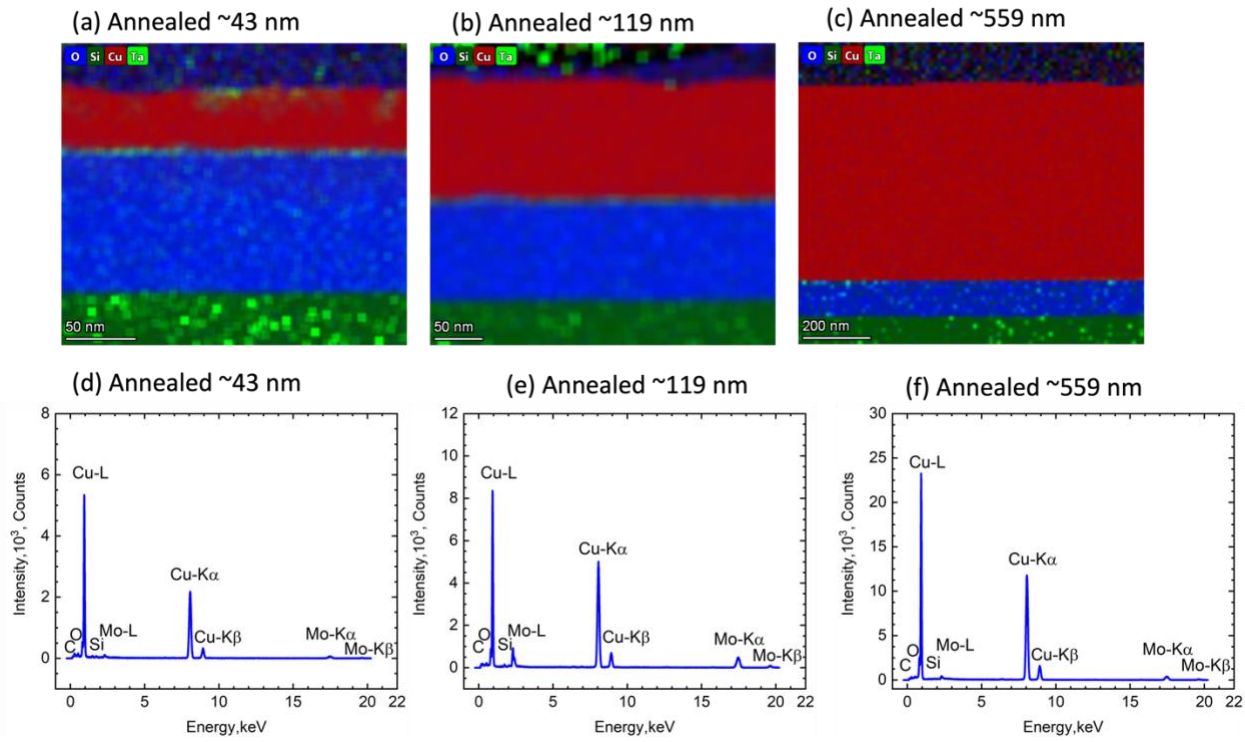

Figure S7: STEM- EDX mapping and spectrum of 43,119 and 559 nm PVD films. The presence of carbon (C) and molybdenum (Mo) in EDX spectrum is related to FIB-SEM and TEM characterization.

Table S2: The atomic fraction of oxygen, silicon and tantalum from EDX analysis on annealed Cu films

PVD films, nm	Oxygen atomic fraction (%)	Silicon atomic fraction (%)	Tantalum atomic fraction (%)	PVD-EP films, nm	Oxygen atomic fraction (%)	Silicon atomic fraction (%)	Tantalum atomic fraction (%)
27	13.2±0.06	2.6±0.14	2.0±0.02	43	8.3±0.11	1.5±0.11	0.08±0.43
57	5.2±0.05	1.11±0.03	0.0	119	3.6±0.03	1.7±0.05	0
119	3.42±0.03	0.59±0.08	0.0	559	6.4±0.06	0.9±0.08	0

We obtain the surface roughness of the films using a Zygo NewView 7300 interference microscope which utilized three-dimensional white-light interferometry, a non-contact profilometry technique. This microscope is equipped with x20 Mirau interference objective, a 150 µm piezo-electric vertical turret, a digital B&W camera (640x480 pixels) and Zygo proprietary image analysis software. The field of view is 350 x 260 µm and the system has a quoted axial resolution of ~ 0.1

nm and <0.3 nm repeatability. The post possessing of measurements was performed by MountainsMap® 6 Analytical to obtain qualitative and quantitative surface roughness.

Figure S8 and S9 shows three-dimensional oblique surface plots of PVD and PVD-EP films. The color bar scale shows the surface roughness variation of the films. However, the average roughness of the PVD and PVD-EP films are almost the same for thickness up to 595 nm as listed in Table S3. The PVD-EP films start to become rougher at 1108 nm and exhibit the highest roughness at 5550 nm thickness.

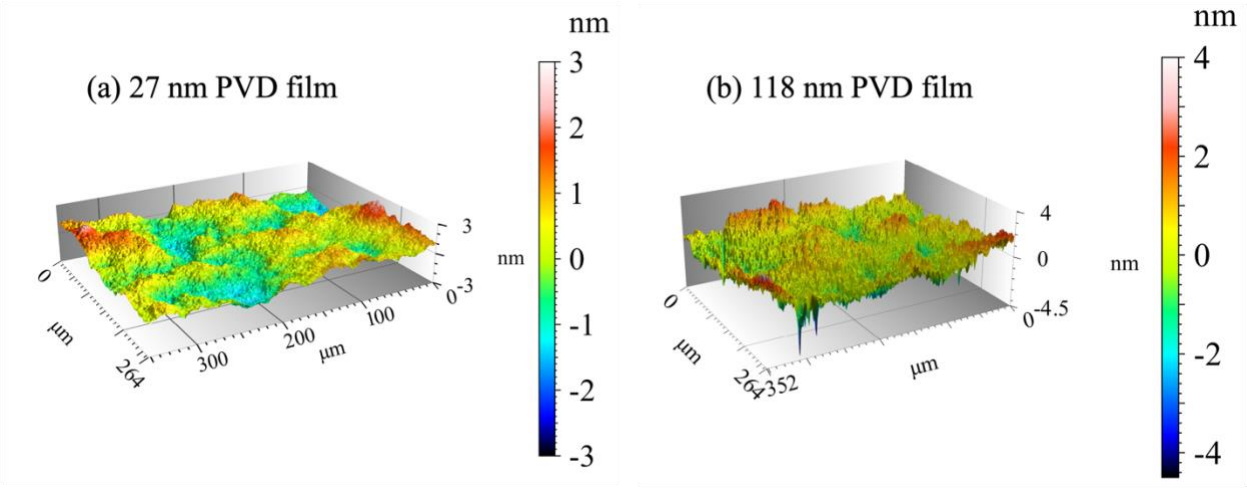

Figure S8: Three-dimensional oblique surface plots of as-deposited PVD films. The color bar scale shows the surface roughness variation of the films.

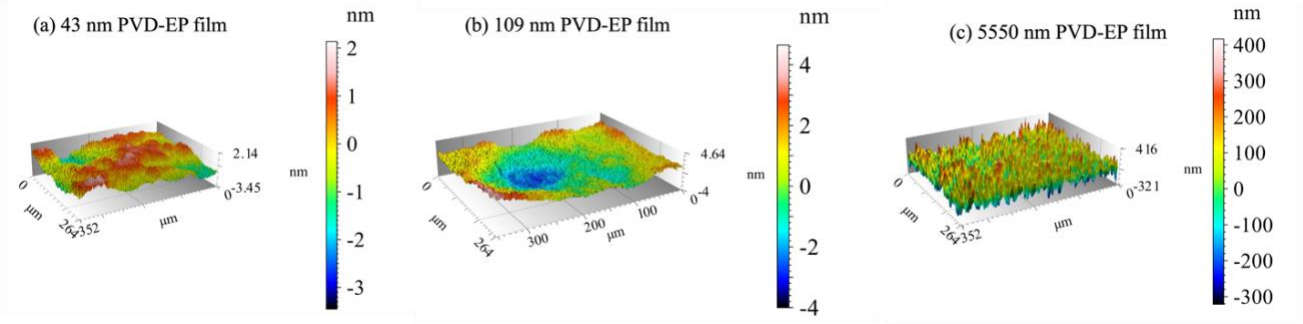

Figure S9: Three-dimensional oblique surface plots of as-deposited PVD-EP films. The color bar scale shows the surface roughness variation of the films.

Table S3: The average roughness of as-deposited PVD and PVD-EP films

PVD film thickness, nm	Average roughness, nm	PVD-EP film thickness, nm	Average roughness, nm
27	0.5085±0.0255	44	0.648±0.076
57	0.4515±0.0065	109	0.909±0.111
118	0.539±0.03	595	0.9605±0.0175
		1108	1.91±0.2
		5550	79.45±0.05

We also confirm the thickness of the Al and Ti transducers using STEM. Note that we use these transducers for steady state and time domain thermoreflectance measurements as discussed in the following sections. The STEM image shown in Figure S10 confirms the thickness of these transducers.

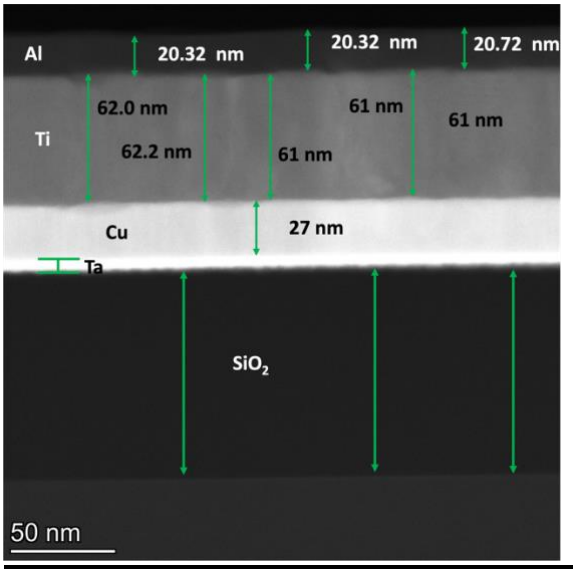

Figure S10: TEM image of 20 nm Al/60 nm Ti coated 27 nm PVD Cu.

S2: First principles-calculation to obtain the thermal conductivity and electron-phonon coupling factor of Cu films

We determine the electron-phonon matrix elements by utilizing the Electron Phonon Wannier (EPW) framework, which is integrated within the Quantum Espresso software package[3]. The Eliashberg spectral function, denoted as $\alpha^2F(\omega)$, characterizes the electron-phonon coupling strength for each phonon mode and is expressed as [4],

$$\alpha^2F(\omega) = \frac{1}{2}\sum_v \int_{BZ} \frac{d\mathbf{q}}{\Omega_{BZ}} \omega_{\mathbf{q}v}\delta\left(\omega - \omega_{\mathbf{q}v}\right), \quad \text{(S1)}$$

here, v signifies the branch index of the phonon wave vector q with its associated frequency $\omega_{\mathrm{q}v}$ and Ω_{BZ} represents the volume of the Brillouin zone, δ serves as a small positive parameter for preserving the correct analytical structure of the self-energies. The electron-phonon coupling strength $\lambda_{\mathrm{q}v}$ for a specific mode v and wave vector q is determined as:

$$\lambda_{qv} = \frac{1}{N(\varepsilon_F)\omega_{\mathrm{q}v}} \sum_{nm} \int_{BZ} \frac{d\mathrm{k}}{\Omega_{BZ}} \times |g_{mn,v}(\mathrm{k},\mathrm{q})|^2 \delta(\varepsilon_{n\mathrm{k}} - \varepsilon_{\mathrm{F}})\delta(\varepsilon_{m\mathrm{k}+q} - \varepsilon_{\mathrm{F}}). \quad \text{(S2)}$$

In this equation, N (ε_{F}) represents the density of states (DOS) of electrons at the Fermi level, $g_{mn,v}$ (k,q) stands for the electron-phonon matrix elements, which describe the scattering of an electron at the Fermi surface from the state nk to the state mk + q, with k being the electron wave vector. The total electron-phonon coupling parameter λ quantifying the overall electron-phonon coupling strength, is evaluated as the Brillouin zone average of the mode-specific coupling strengths $\lambda_{\mathrm{q}v}$,

$$\lambda = \sum_{\mathrm{q}v} \omega_{\mathrm{q}} \lambda_{\mathrm{q}v}, \quad \text{(S3)}$$

here, ω_{q} represents the Brillouin zone weights associated with phonon wave vectors q, which are normalized to 1 within the Brillouin zone. To ensure the accurate computation of Equation (S3), it is imperative to employ dense grids of k and q in the Brillouin zone. This is accomplished by interpolating electron-phonon matrix elements, phonon modes, and band energies from an initial coarse grid (10 × 10 × 10 and 5 × 5 × 5) to a uniform fine grid (80 × 80 × 80 and 35 × 35 × 35) for electron and phonon wave vector grids, respectively. The interpolation process leverages maximally localized Wannier functions derived from Bloch energy bands[5]. In these calculations, we utilize norm-conserving pseudopotentials obtained from the PS Library for Cu [6].A plane wave cutoff of 1632.7 eV (120 Ry) is implemented for these computations.

We calculate the Eliashberg spectral function $\alpha^2F(\omega)$ for Cu at room temperature from our density functional perturbation theory calculation as shown in Figure S11 which also includes the calculation of the corresponding mass enhancement factor, λ. At room temperature, we calculate the λ to be ~0.13, which matches well with previous calculations[7] . We also calculate the electron-phonon scattering rate for Cu at room temperature from our parameter free DFPT calculation as shown in Figure S11b. From the calculated scattering rates, we calculate the average mean free path (Λ) of Cu at room temperature to be ~39 nm which is in excellent agreement with prior theoretical calculation [8].

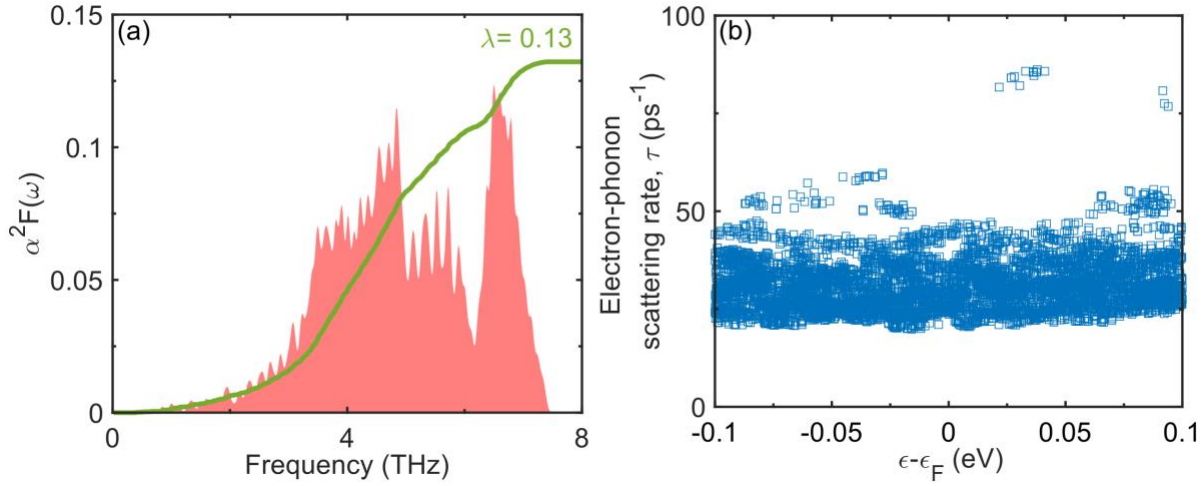

Figure S11:(a) Calculated Eliashberg Spectral function, $\alpha^2F(\omega)$, for Cu at room temperature. The solid line indicates the corresponding mass enhancement factor. (b) Calculated scattering rate of electrons due to electron-phonon scattering for Cu at room temperature. From the calculated scattering rates and the Fermi velocity, we derive the average mean free path of the electrons at Fermi level.

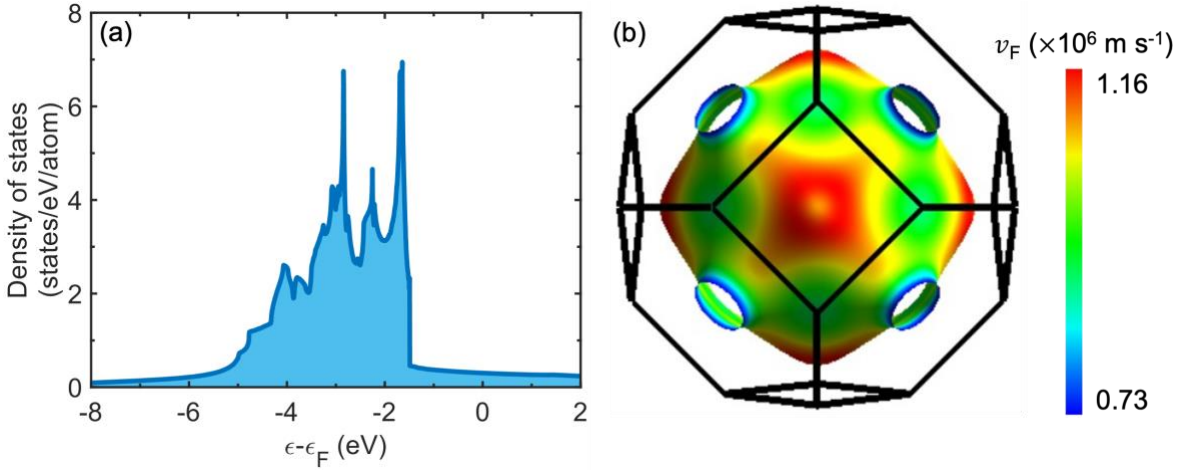

Figure S12: Calculated electronic density of states for Cu ate room temperature. The calculated density of states gives an insight into the electronic configuration of the metal. (b) Calculated Fermi surface of Cu at room temperature. The color on the surface represents the Fermi surface.

We calculate the electronic density of states (eDOS) for Cu with Qunatum Espresso using tetrahedron method with **k**-point grid of 50 × 50 × 50. Figure S12 (a) shows the eDOS for Cu at room temperature. The high-density region associated with *d*-bands is located ~2-4 eV below the Fermi level in the eDOS[9] . We also calculate the Fermi surface of Cu with Quantum Espresso using a dense k-grid of 120 × 120 × 120. The color on the Fermi surface is representative of the Fermi velocity. We calculate the average Fermi velocity to be ~1.05 × 10^6 m s^{-1}, which is in close agreement with previous theoretical calculation[8].

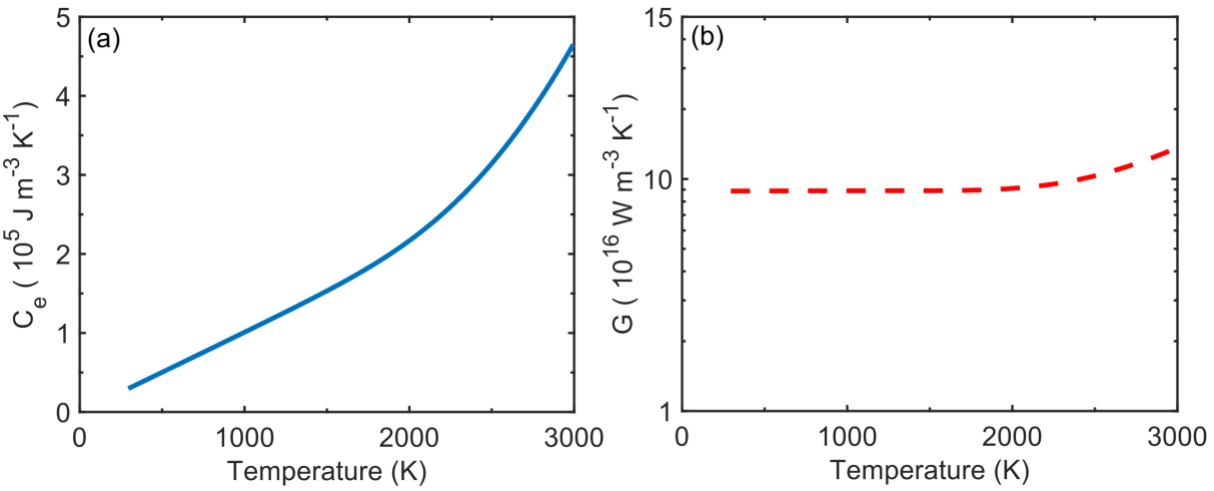

Figure S13:(a) Temperature dependent electronic heat capacity, $C_e(T_e)$, of Cu. (b) Temperature dependent volumetric electron-phonon coupling factor, $G(T_e)$ for Cu.

We calculate the temperature dependent electronic heat capacity of Cu using the derivative of the total energy density with respect to T_e, and is given as,

$$C_e(T_e) = \int_{-\infty}^{\infty} \frac{\partial f(\varepsilon,\mu,T_e)}{\partial T_e}\, g(\varepsilon)\varepsilon d\varepsilon, \quad \text{(S4)}$$

where $g(\varepsilon)$ is the eDOS at the energy level ε, μ represents chemical potential at T_e, and $f(\varepsilon,\ \mu,\ T_e)$ denotes fermi distribution function, defined as $f(\varepsilon,\mu,T_e) = \{\exp[(\varepsilon-\mu)/k_B T_e] + 1\}^{-1}$.
We also calculate the temperature dependent volumetric rate of e-p coupling, which is given as,[9]

$$G = \pi\hbar k_B \lambda\langle\omega^2\rangle \int_0^{\infty} \frac{(D(\varepsilon))^2}{D(\varepsilon_F)}\left[-\frac{\partial f}{\partial \varepsilon}\right] d\varepsilon, \quad \text{(S5)}$$

where $\langle\omega^2\rangle$ denotes the second moment of the phonon spectrum and $D(\varepsilon)$ represents the eDOS. At room temperature, the calculated G is ~8×10^{16} W m^{-3} K^{-1}, which matches closely with previous caculations[10] . From the calculated C_e, v_F and Λ, we calculate the thermal conductivity as detailed in our previous works [11].
We calculate the thermal conductivity of Cu at room temperature to be ~400 W m^{-1} K^{-1}, which is in excellent agreement with our experimental measurements. We introduce the effect of boundary scattering on the total scattering rate of the electrons as,[12]

$$\frac{1}{\tau_{tot}} = \frac{v_F}{\Lambda} + \frac{v_F}{d} \quad \text{(S6)}$$

where d is the thickness of the thin film and τ_{tot} is the total scattering rate which includes electron-phonon scattering rate as well as the boundary scattering of the electrons. Here, we consider that the electrons scatter primarily with phonons at room temperature and do not consider electron-electron scattering.

S3: TDTR thickness, sensitivity, uncertainty, and data analysis

To support SSTR measured in-plane thermal conductivity, we measure various thermophysical properties of our films using the time-domain thermoreflectance technique (TDTR). In this technique, a Ti: sapphire laser (Spectra Physics Tsunami) with a central wavelength of ~808 nm operates at 80 MHz repetition rate and is spilt into a pump beam and a probe beam. We modulate the pump beam at a frequency of our interest employing an electro-optic modulator (EOM) in its

path. This beam modulation produces a periodic temperature rise on the surface of a sample which changes its reflectivity. The probe beam detects this change in reflectivity of the sample surface using a balanced photodetector and a lock-in amplifier. To obtain the spot size of the pump and probe beams at 20X magnification, we utilize our calibration sample: Al coated high purity fused silica (Corning HPFS 7980, 1.36 $Wm^{-1}K^{-1}$). We measure the change in reflectivity of this calibration and then plug its known thermal conductivity as an input to our thermal model; the spot size is adjusted to obtain the expected thermal conductivity of calibration. Applying this method, an effective radius of ~2.15 μm is obtained for the pump and probe beams. We assume that both beams have the same size during spot size analysis since our thermal model takes their geometrically weighted average. We measure the thermal conductivity of another calibration sapphire to confirm this spot size.

We perform picosecond ultrasonics on Al coated as-deposited Cu films. The details of picosecond ultrasonics is described elsewhere [13,14]. Briefly, in picosecond ultrasonic measurements, the laser pulse is absorbed on Al surface which launches mechanical strain waves from the surface to the underlying layers. These strain waves travel at the speed of sound in the corresponding layer. These waves are partially reflected and partially transmitted at the interface between the layers, depending on their acoustic impedance defined as $[Z = (\rho \times E)^{\frac{1}{2}}$ where ρ is density and E is Young's modulus]. When there are a few number of layers and the acoustic impedance mismatch is large, the strain waves are mostly reflected. The reflected waves from each interface travel back to the surface and impact the thermoreflectivity of the transducer. We detect this reflected echoes using the probe beam as troughs or peaks. Figure S14 shows the acoustic impedance at the Al/Cu interface is sufficiently large to influence our TDTR signal. In this case, the peaks correspond to the reflected waves from the Al/Cu interface. There is a dip indicated by solid vertical line in the thermoreflectivity decay curve which appears because of the strain wave reflecting off a Cu/SiO_2 interface to the surface. We can use this information to determine the sound speed and elastic propertie of the Cu layer with the knowledge of TEM thickness. The 3 nm Ta does not have a noticeable impact on the transmission of strain waves between Cu and SiO_2 interface. The strain waves are reflected off the Cu/ SiO_2 interface. The echoes in the thermal decay curve are shifting to the right (longer times) with an increase in Cu film thickness indicating by the arrow. However, the dips from Cu/ SiO_2 interface are not detectable at ~595 nm thick film and beyond.

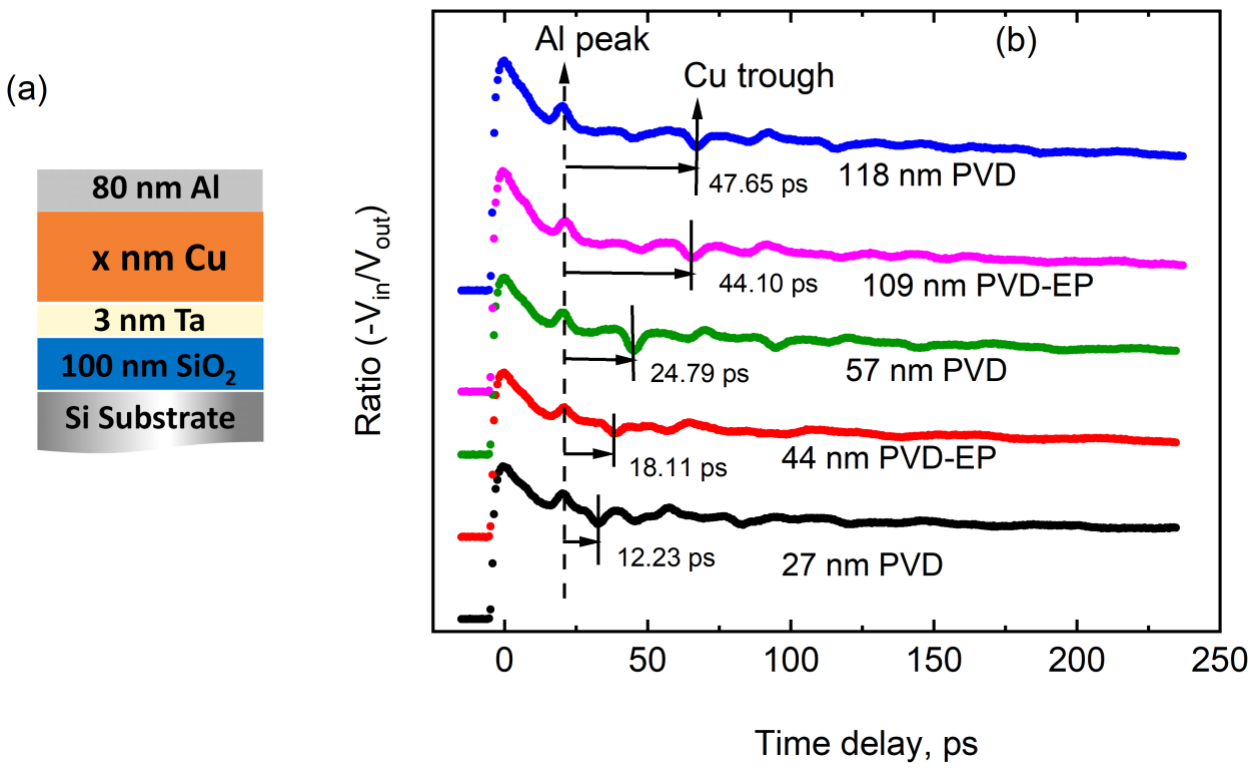

Figure S14: (a) Schematic for the film layers configuration studied here. (b)TDTR thermal decay signals showing the picosecond ultrasonic echoes from different interfaces for the as-deposited Cu films.

To increase the sensitivity of our TDTR measurement to the in-plane thermal conductivity of the Cu films, we use a 20 nm Al/60 nm Ti transducer. The total thickness of this transducer ensures optical opacity, the top 20 nm of Al ensures a large probe thermoreflectance response, and 60 nm Ti reduces the thermal conductivity of the transducer to maximize heat spreading in the Cu layer relative to the transducer. We determine thermal conductivity of 20 nm Al and 60 nm Ti from Al/Ti coated Al_2O_3 and SiO_2 calibrations at ~2.15 μm effective radius. This spot size makes the experiments sensitive to the thermophysical properties of Al/Ti coated calibrations. We use a three-layer heat diffusion model to determine the thermal conductivity of Al and Ti [15–17] . Figure S15 exhibits the best-fit thermal model to the ratio of the in-phase and out-of-phase signal ($-V_{in}/V_{out}$) data fitting for the thermal conductivity of calibrations and thermal boundary resistance of Ti/calibrations. We adjust the thermal conductivity of the Al and Ti until we obtain the known thermal conductivity of the calibrations listed in Table S4. We assume the thermal boundary resistance between Al/Ti to be 3.3×10^{-10} K m^2 W^{-1} [18–20]. To fit the experimental data with the model we use the thermophysical properties of Al, Ti, Al_2O_3 and SiO_2 listed in Table S4. The calculated thermal conductivity of Al is 110 W m^{-1} K^{-1} and Ti is 19 W m^{-1} K^{-1}. We verify their thermal conductivities using four-point probe technique. Using this technique, we measure the effective electrical conductivity of 20 nm Al and 60 nm Ti from Al/Ti coated Al_2O_3. We apply Wiedemann-Franz law assuming Lorenz number of 2.44×10^{-8} V^2 K^{-2} on the effective electrical conductivity to obtain the effective thermal conductivity of Al and Ti. The effective thermal conductivity of Al and Ti is 36.20 W m^{-1}K^{-1} which is comparable to TDTR measured effective thermal conductivity.

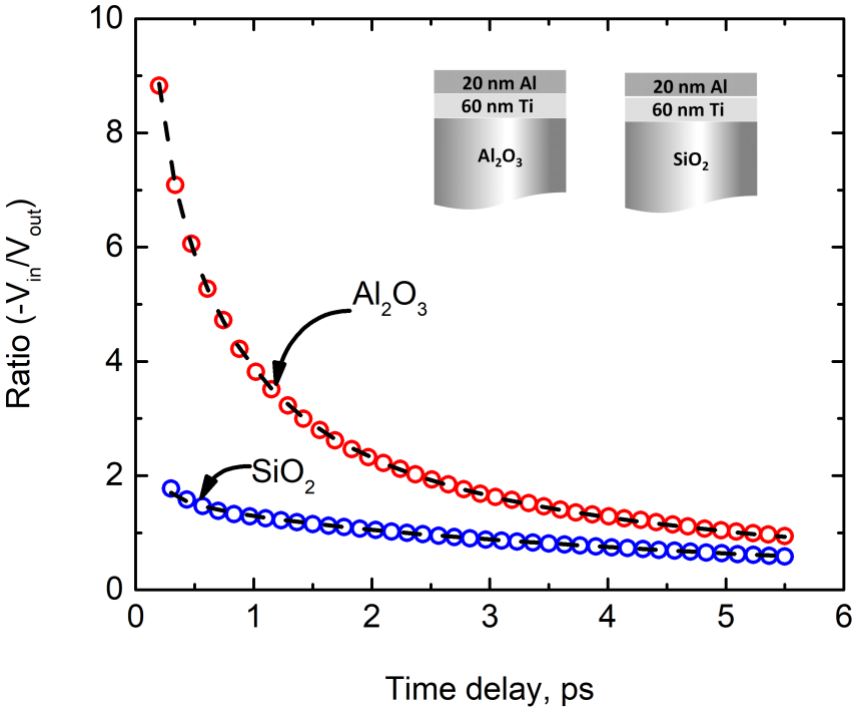

Figure S15: Fit of TDTR experimental data for Al/Ti/Al_2O_3 and Al/Ti/ SiO_2.

To verify if the TDTR measurements are sensitive to the in-plane thermal conductivity of the Cu films, we perform a sensitivity analysis. We calculate the sensitivity to in-plane thermal conductivity of thinnest film: 27 nm Cu at two spot sizes and modulation frequencies. For these calculations we use various thermophysical properties of each layer listed in Table S4. Figure S16a shows that the sensitivity to the in-plane thermal conductivity of 27 nm Cu is higher at 1.2 MHz and 2.15 μm effective radius. The sensitivity is higher at 1.2 MHz and 2.15 μm effective radius due to deeper thermal penetration depth as shown in Figure S16[21]. TDTR measurements are highly sensitive to the thermal conductivity of SiO_2 and Si compared to in-plane thermal conductivity of 27 nm as shown in Figure S16c. We use the accepted literature values of SiO_2 and Si[1,22–25] in our thermal model to fit the experimental data. The sensitivity to in-plane thermal conductivity increases with thickness as shown in Figure S16d. The cross-plane conductivity of Cu films has lower sensitivity relative to in-plane. However, we determine this cross-plane thermal conductivity using TDTR at different experimental conditions discussed below.

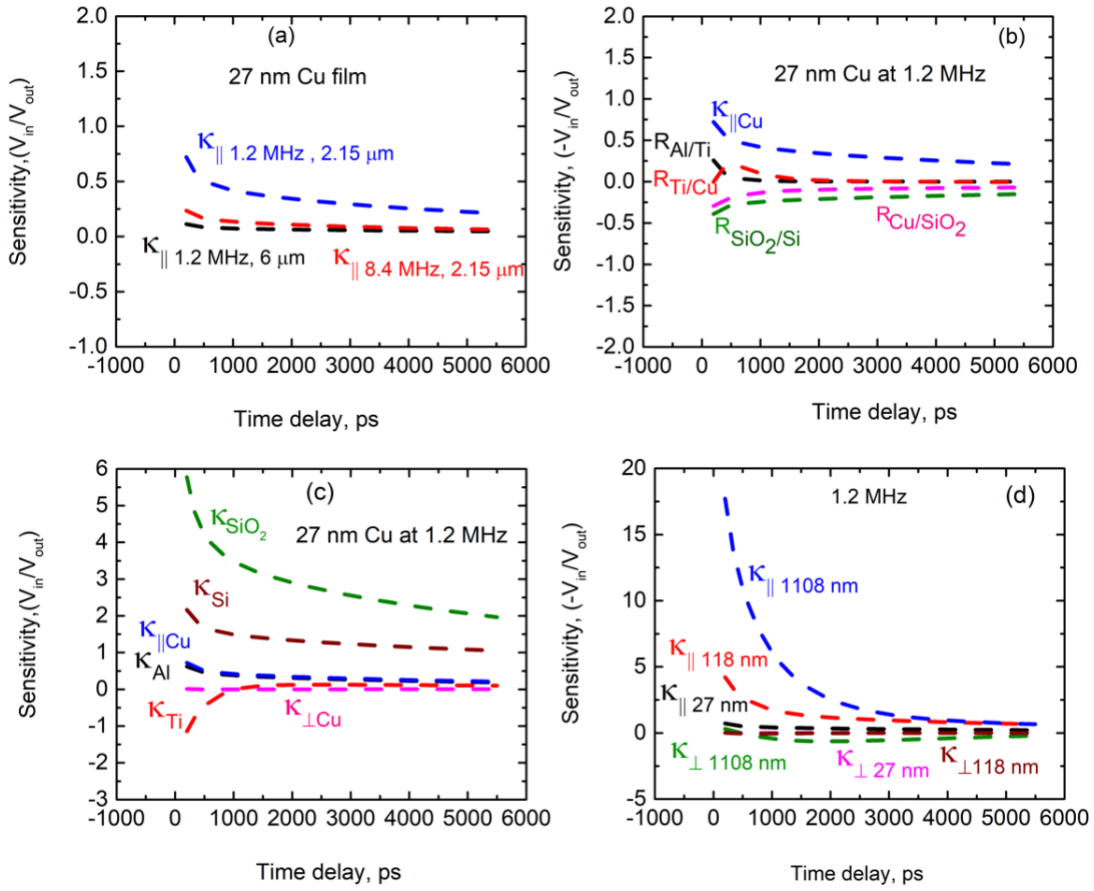

Figure S16: (a) TDTR measurement sensitivities to the in-plane thermal conductivity ($\kappa_{\parallel}$) of Al/Ti coated 27nm PVD Cu at different modulation frequencies and effective radii of beam. (b and c) The sensitivity to in-plane thermal conductivity of 27 nm PVD Cu relative to various thermal parameters in our sample stack. (d) The sensitivity to the cross-plane ($\kappa_{\perp}$) and in-plane thermal conductivity ($\kappa_{\parallel}$) of Cu films. The sensitivity to ($\kappa_{\parallel}$) increases with film thickness.

To determine the in-plane thermal conductivity of Cu films, we use a five-layer heat diffusion model[15–17] . Figure S17 exhibits the best-fit thermal model to the ratio of the in-phase and out-of-phase signal ($-V_{in}/V_{out}$) data fitting for the in-plane thermal conductivity of Cu films. The thermophysical properties and thicknesses of different layers used in thermal model are listed in Table 1 (main manuscript) and S4. The cross-plane thermal conductivity of Cu shown in Figure S21 is also used as input variable in the thermal model. Figure S18 shows the residual contours for our model's fit relative to the best-fit with respect to the calculated in-plane thermal conductivity and thermal boundary resistance between Ti and Cu ($R_{Ti/Cu}$). We notice that for a wide range of different values for in-plane thermal conductivity and thermal boundary resistance can be used to fit our model to the experimental data. We choose 2.5% residual threshold where the thermal model generates the same quality of fit to the experimental data. The quality of fit based on the model parameters and experimental data is within 2.5% threshold value indicating that TDTR is sensitivite to the in-plane thermal conductivity. We include this 2.5% residual

uncertainty along with spot to spot thermal conductvity variations in our total uncertainty calcultion following equation: Total uncertainty (ε_i),

$$\varepsilon_i = \sqrt{(\sigma_i{}^2) + \sum_i \Delta_i^2} \quad \text{(S7)}$$

Here σ_i represents the standard deviations among multiple measurements across various spots and Δ_i is the uncertainty associated with an individual parameter of the thermal model[22,26]. The TDTR measured thermal conductivities of as-deposited and annealed are shown in Figure S21 which we discuss in the following section.

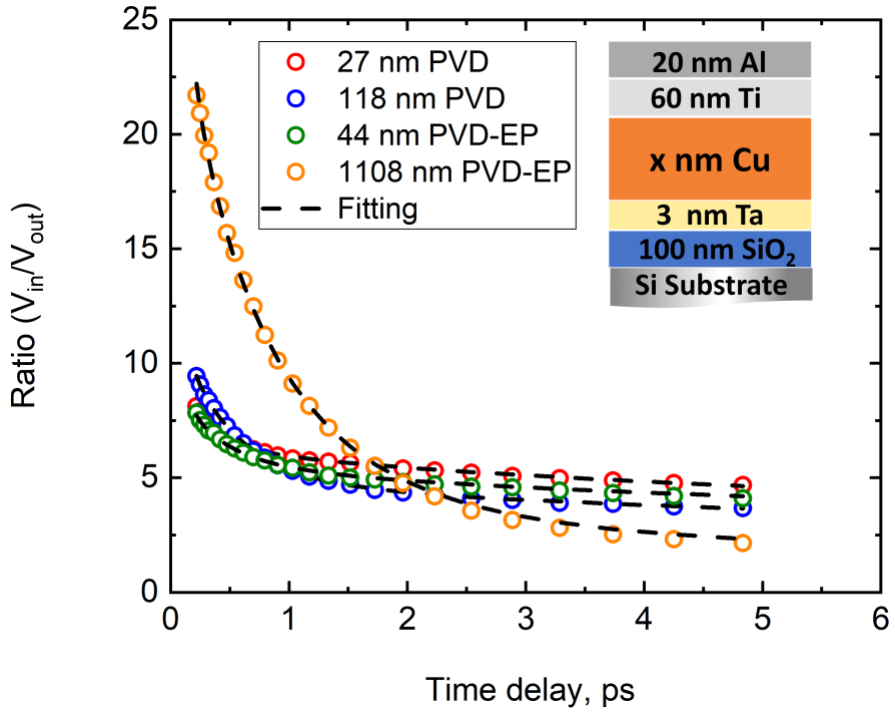

Figure S17: Theoretical fit of experimental data for as-deposited 27 nm PVD, 44 nm PVD-EP Cu, 118 nm PVD and 1108 nm PVD-EP Cu films

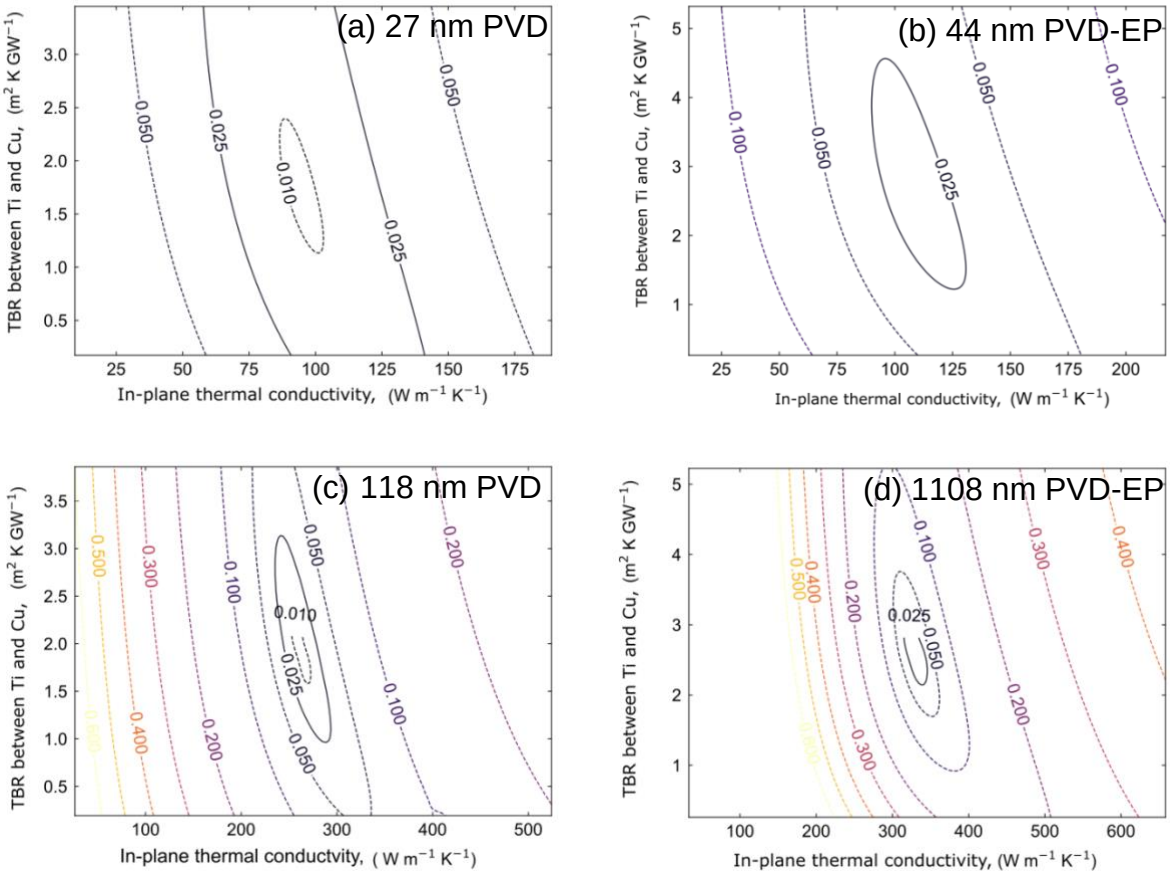

Figure S18: Residual contours of our model's fit relative to the best fit for different thick Cu films as a function of in-plane thermal conductivity. We choose 2.5% residual threshold within which the thermal model generates the same quality of fit to the experimental data.

TDTR measurements also benefit through the use of the Al/Ti transducer to resolve the in-plane thermal conductivity of Cu relative to using a pure Al transducer (Figure S19). Al/Ti coated Cu films exhibit at least 3.5 times lower uncertainty than that of Al coated Cu films in TDTR measurements implying that Al/Ti coated samples have higher sensitivity to the in-plane thermal conductivity.

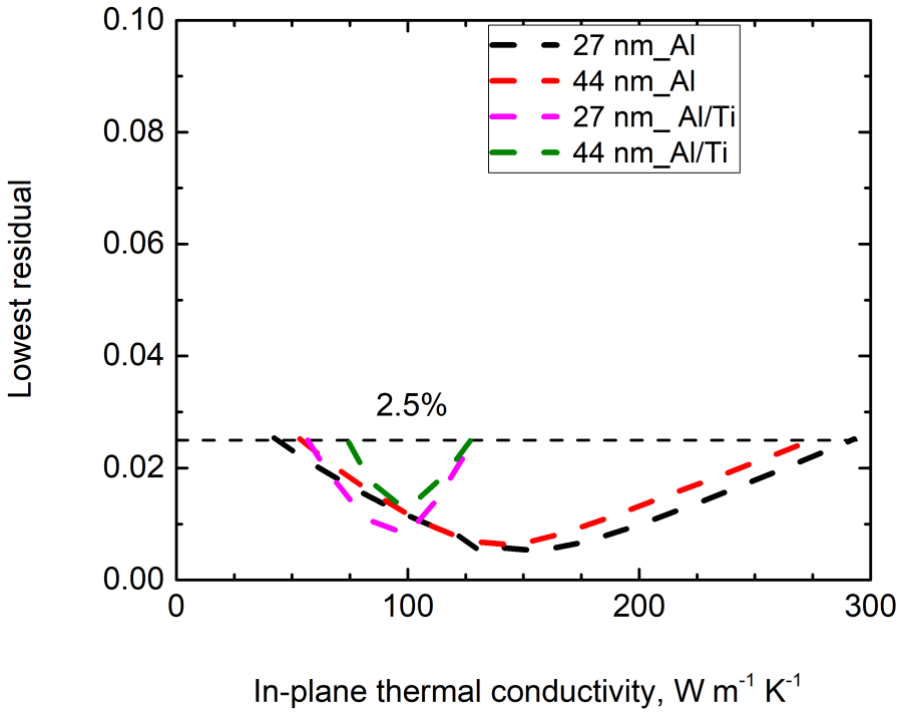

Figure S19: 2D contour analysis Al and Al/Ti coated as-deposited Cu films assuming the quality of fit based on the model parameters and experimental data is within 2.5% threshold value.

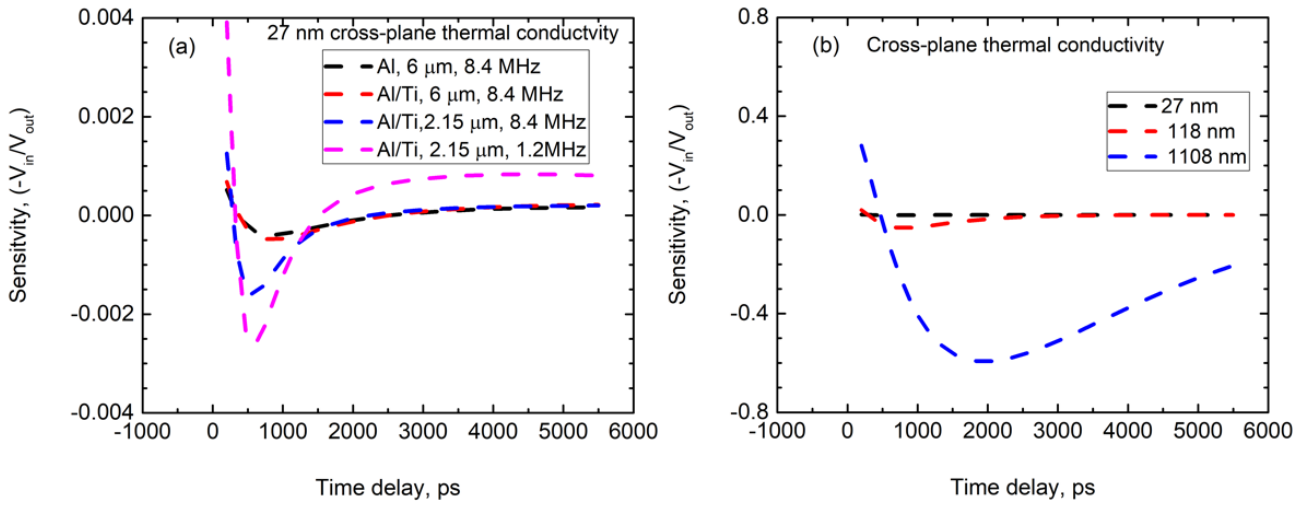

Figure S20: (a) TDTR sensitivity to the cross-plane thermal conductivity of 27nm PVD Cu at different modulation frequencies, effective radii of beam, Al and Al/Ti transducers. (b) The sensitivity to cross-plane thermal conductivity of different thick Cu films. The sensitivity increases with film thickness.

We also determine the cross-plane thermal conductivity of Cu using TDTR technique. First, we determine the sensitivity of cross-plane thermal conductivity to different modulation frequencies, spot sizes and two different transducer properties. We expect that the larger spot size and transducer with high thermal conductivity, such as Al, would reduce the heat spreading in the in-

plane direction of Cu layer and hence increase the sensitivity to cross-plane thermal conductivity. However, having Al and 6 μm effective radius beam size, we do not find high sensitivity to cross-plane thermal conductivity of Cu as shown in Figure S20a. Rather we find that 27 nm Cu film is closely sensitive to cross-plane thermal conductivity having Al/Ti transducer at 1.2 MHz and 8.4 MHz with the tight spot size of 2.15 μm radius. Indeed, the film is more sensitive to cross plane thermal conductivity at 1.2MHz. However, at this frequency we are highly sensitive to in-plane thermal conductivity as shown in Figure S16(c) and (d). Therefore, to have less interdependence of in-plane thermal conductivity in determining the cross-plane thermal conductivity we choose 8.4 MHz and 2.15 μm effective radius. Figure S20b depicts that the sensitivity to cross-plane thermal conductivity increases with thickness.

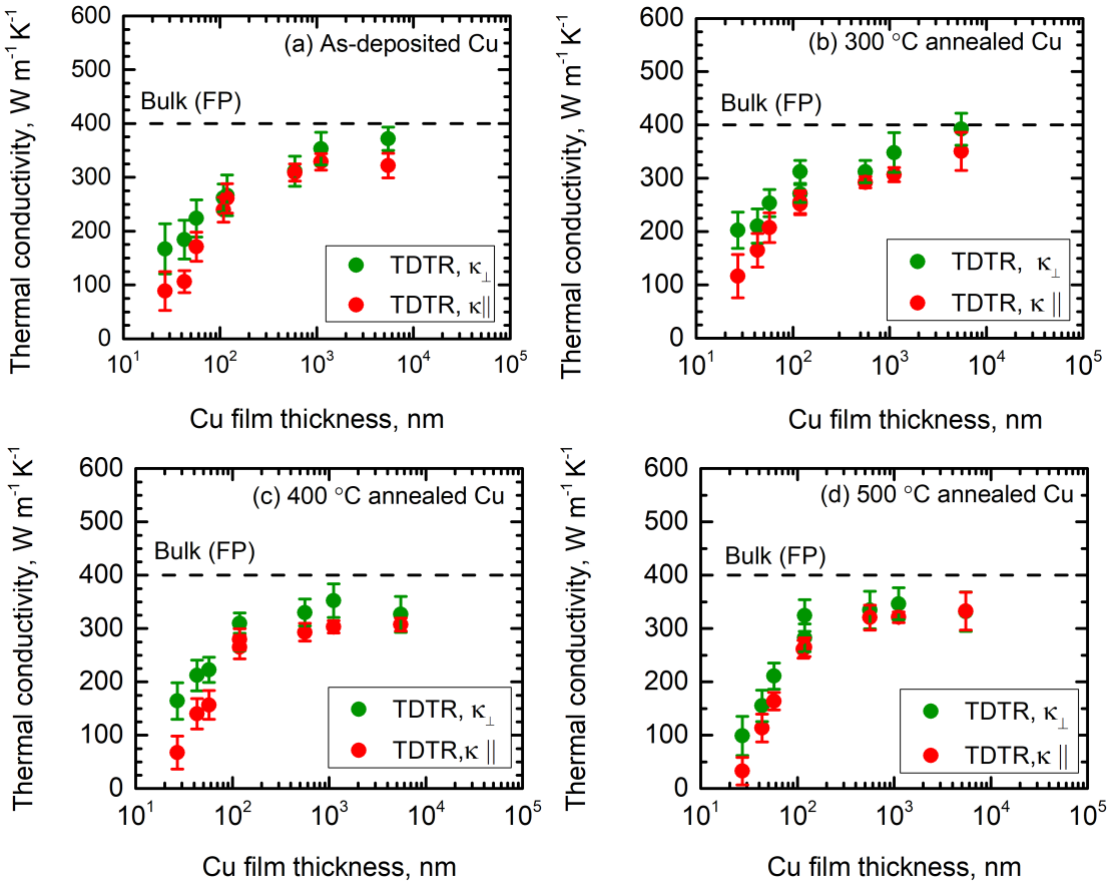

Figure S21: (a), (b), (c) and (d) comparison of TDTR measured cross-plane ($\kappa_\perp$) and in-plane thermal conductivity ($\kappa_\parallel$) of as-deposited and annealed Cu films. The dashed line represents the calculated bulk thermal conductivity of Cu from our first principles (FP) calculations.

Figure S21 shows the cross-plane and in-plane thermal conductivity of as-deposited and annealed Cu films. We determine the cross-plane thermal conductivity of Cu following the same procedure of in-plane thermal conductivity discussed above. In the thermal model, we fit for cross-plane thermal conductivity and thermal boundary resistance of Ti and Cu. Indeed, Figure S21 shows that the cross-plane and in-plane thermal conductivity comply for film thickness of 50 nm to 5 μm.

There is a slight discrepancy in the thermal conductivities of 27 and 43 nm films, which we hypothesize is due to the microstructure of the Cu films.

Table S4: Parameters used in sensitivity analysis and the thermal model to determine the in-plane and cross-plane thermal conductivities of the Cu films.

Materials	Thickness, nm	Heat capacity, $MJm^{-3}K^{-1}$	Thermal conductivity, $W\ m^{-1}\ K^{-1}$	Thermal boundary resistance, (TBR) $m^2\ K\ GW^{-1}$
Al	20	2.42 [1]	110	
Al/Ti	--	--	--	0.333[18–20]
Ti	60	2.36[27]	19	
Al_2O_3		3.06[27]	34±1.5 [22,28]	
Ti/Al_2O_3	--	--	--	~2.78-2.94
Ti/Cu	--	--	--	TDTR best fit values[b]
Cu	27 nm-5 μm	3.45[1]	TDTR determined cross-plane thermal conductivity[a]	
Cu/SiO_2				5.00 [24]
SiO_2	100	1.62 [22–24]	1.35[1,22,24,25]	
SiO_2/Si	-	-	-	4.35 [23,24]
Si	-	1.65 [1,22–25]	130 [22,24]	-

a. Figure S21 shows the cross-plane thermal conductivity of Cu determined with TDTR.
b. We utilize the TDTR best-fit to determine the in-plane thermal conductivity using SSTR.

S4. SSTR sensitivity, uncertainty and data analysis

Like TDTR measurements, a 20 nm Al/60 nm Ti transducer increases the sensitivity of our SSTR measurement to the in-plane thermal conductivity of the Cu films.

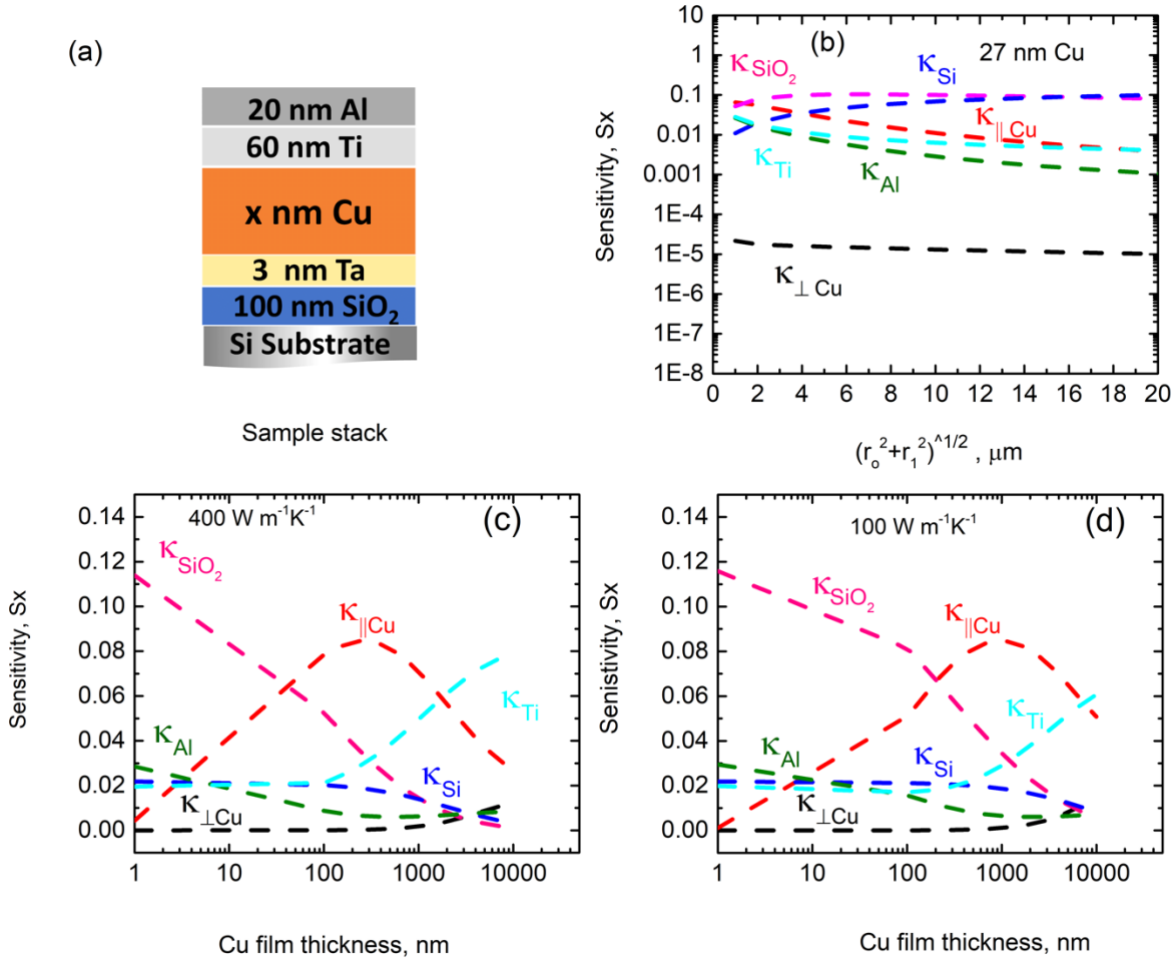

Figure S22: (a) Typical sample stack of Cu film with an Al/Ti transducer. [(b), (c) and (d)] SSTR sensitivity to different parameters of a five-layer model for 27 nm PVD Cu as a function of spot sizes and Cu film thickness. [(c) and (d)] the analysis is performed at an effective radius ($\sqrt{r_0^2 + r_1^2}$) *of 2.22 μm. The sensitivity to in-plane thermal conductivity* ($\kappa_\parallel$) *of Cu films is higher than its cross-plane thermal conductivity* ($\kappa_\perp$)

To verify if the SSTR measurements are sensitive to the in-plane thermal conductivity of the Cu films, we perform a sensitivity analysis. We calculate the SSTR sensitivities (S_x) to various thermal parameters in our samples with respect to the spot sizes and Cu film thicknesses following an approach similar to that of Braun et al. and Yang et al. [22,29]

$$S_x = \frac{\Delta T_{1.1x}(r_{01}) - \Delta T_{0.9x}(r_{01})}{\Delta T_x(r_{01})} \quad \text{(S8)}$$

$$S_x = \frac{\Delta T_{1.1x}(thickness) - \Delta T_{0.9x}(thickness)}{\Delta T_x(thickness)} \quad \text{(S9)}$$

Here ΔT_x is the temperature rise calculated by the steady-state thermal model for the input variables. In equation S8, the input variables are *x* and effective radius, $r_{01}=\sqrt{(r_0^2 + r_1^2)}$, where r_o and r_1 are the pump and probe radii. For equation S9, the input variables are the thicknesses of Cu film. The values presented in Table S4 are used as input variables. Figure S22b exhibits that the sensitivity of cross-plane conductivity ($\kappa_\perp$) and in-plane thermal conductivity ($\kappa_\parallel$) of 27 nm PVD Cu films along with other thermal parameters in this sample. Figure S22b exhibits that a tight beam size results in a higher sensitivity to the in-plane thermal conductivity, determined for the 27 nm PVD Cu film. The sensitivity calculation for this sample indicates that the sensitivity to the in-plane thermal conductivity of 27 nm Cu is sufficient when the effective radius is ~2.0-4.0 μm. However, Figure S22b also indicates that the sensitivity to the thermal conductivity of SiO_2 is slightly higher than the in-plane thermal conductivity of 27 nm around these spot sizes. To extract in-plane thermal conductivity of Cu, we use widely accepted thermal conductivity of SiO_2 = 1.35 $Wm^{-1}K^{-1}$ [1,22,24,25] in our thermal model. The sensitivity to thermal conductivity of SiO_2 decreases with increasing Cu film thickness as shown in Figure S22(c) and (d). We generate Figure S22(c) and (d) assuming $\kappa_{\perp Cu} = \kappa_{\parallel Cu}$ = 400 W m^{-1} K^{-1} and 100 W m^{-1} K^{-1}, respectively. The analysis is performed at an effective radius of ~2.22 μm, a typical pump and probe spot size in our fiber SSTR system. Figure S22(c) and (d) displays that the sensitivity to in-plane thermal conductivity is higher than that of cross-plane up to 1 μm. This is because Cu thin film has higher thermal conductivity than that of the SiO_2, which leads to the heat flowing predominantly along the in-plane direction of the Cu film[22,30] .As a result, the temperature gradient along the in-plane direction is much more pronounced compared to cross-plane one. Therefore, in our case, the in-plane thermal conductivity of Cu film dominates the sensitivity calculations allowing SSTR to measure the in-plane thermal conductivity. We determine this cross-plane thermal conductivity of Cu using TDTR (Figure S21) to apply in the thermal model of SSTR. One more notable feature of Figure S22(c) and (d) is that the sensitivity of thermal conductivity of Al and Ti is higher than that of cross-plane thermal conductivity of Cu, specifically thermal conductivity of Ti increases for film thickness beyond ~100 nm. We measure the thermal conductivity of Al and Ti using TDTR as described in the previous section. We also use widely literature value for the thermal conductivity of Si as shown in Table S4. The heat capacity and thermal boundary resistances for the sensitivity calculations were taken from the literature[1,22,23,27] .

To determine the in-plane thermal conductivity of the Cu films in SSTR measurements, we fit for the in-plane thermal conductivity while other materials' properties are either independently determined via TDTR or assumed from the literature which are listed in Table S4. Figure S23 presents △V/V vs △P which we use in SSTR fitting to extract the thermal conductivities of sapphire and as-deposited Cu films. The details of the procedure are discussed in Braun et al. [22]. Typically, we determine γ from our sapphire calibration sample, with known thermal properties of transducer and sapphire listed in Table S4. The assumption here is that γ does not change between the samples of interest. After determining γ from the reference sample, we calculate the thermal conductivity of Al/Ti coated Cu films by the steady-state thermal model. The thermal conductivities of the Cu films are analyzed with a five-layer model: Al/Ti transducer/Cu thin film/SiO_2/Si substrate. During modeling we utilize thickness and thermophysical properties of Cu film stacks listed in Table 1 (main manuscript) and Table S4.

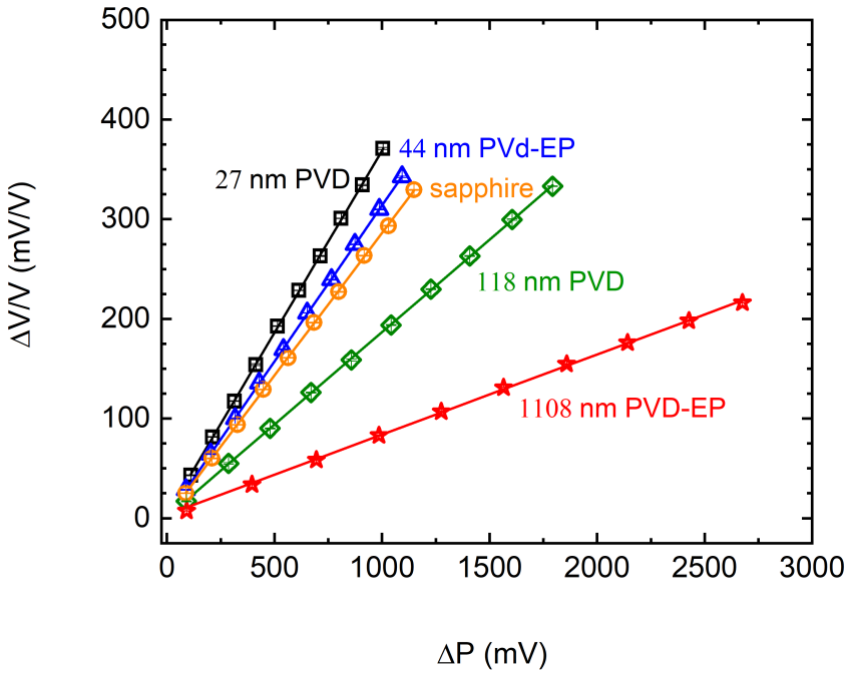

Figure S23: $\Delta V/V$ vs. ΔP ($\propto$ pump power) used in SSTR fitting to extract the thermal conductivities of sapphire and Cu films measured with an effective radius of ~2.22 μm *(20X magnification)*

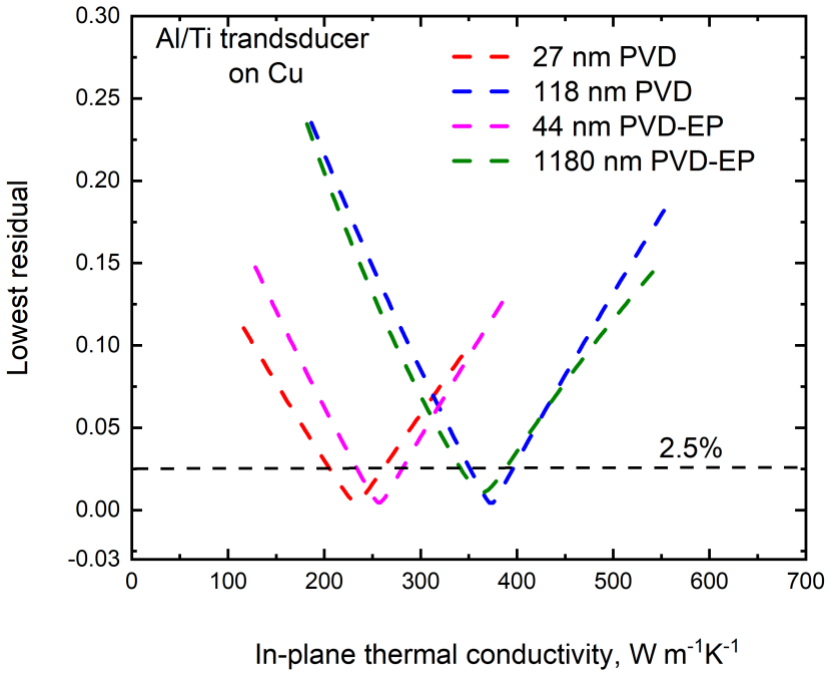

Figure S24: 2D contour analysis of different thick Cu films assuming the quality of fit based on the model parameters and experimental data is within 2.5% threshold value.

Since there is considerable sensitivity to various thermal parameters, we employ a type of contour plot to characterize the similarity of various fits between the experiment and thermal model to determine the interdependence of parameters while extracting in-plane thermal conductivity of Cu. We compare our measued SSTR data to the results of a thermal model where we iterate the in-plane thermal condutivity of the Cu to achieve a best fit. Figure S24 shows the quality of the fit within the 2.5% residual indicating the ability of SSTR to measure the in-plane thermal conductivity. We choose this thresold value depending on the data quality at which the model could be in definitely disagreeement with the experimental data[26,31] .The residual values for best fit thermal conductivity at 2.5% represent the uncertainty in determining the in-plane thermal conductivity based on the film thicknesses and thermophysical parameters of each layer. The error bars presented in the manuscript and Figure S26 are calculated by equation S7. In our total uncertainty calculations, we include 2.5% residual uncertainty and thermal conductivity variations at different spots for multiple measurements.

We perform the same residual analysis on SSTR measured Al coated Cu films to assess the benefit of using the Al/Ti transducer to resolve the in-plane thermal conductivity of Cu relative to using an Al transducer. As shown in Figure S25, the use of an Al transducer results in at least 2 times higher uncertainty in determining the in-plane thermal conductivity of the Cu films relative to Al/Ti transducers.

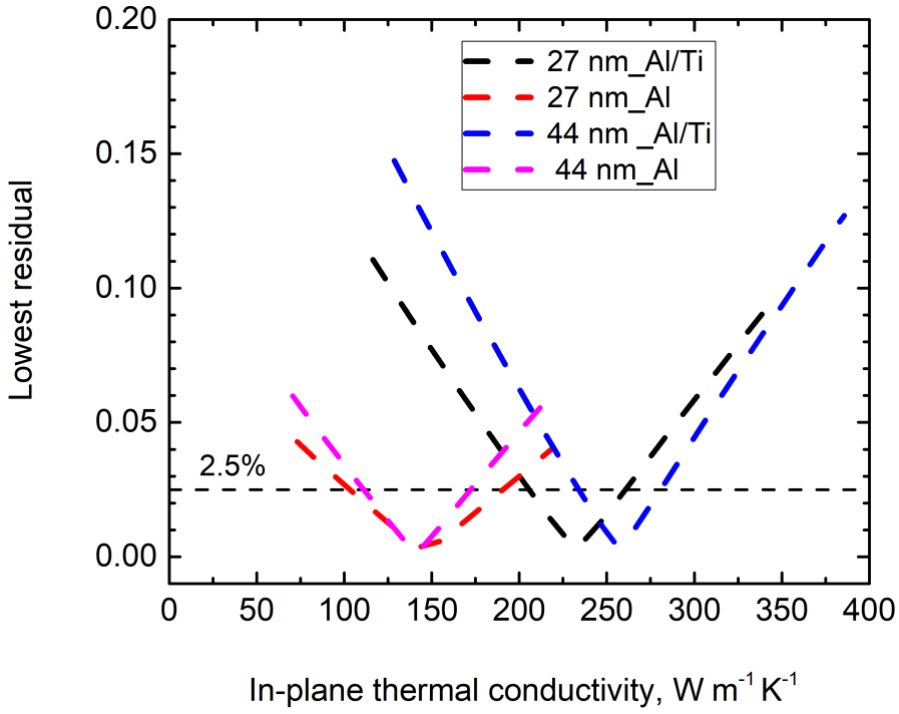

Figure S25: 2D contour analysis comparison of Al and Al/Ti coated Cu films of different thicknesses assuming the quality of fit based on the model parameters and experimental data is within 2.5% threshold value.

S5. Comparison of SSTR, TDTR, and four-point probe measured thermal conductvities of Cu films

Figure S26 shows the in-plane thermal conductivity of as-deposited and annealed Cu films measured with four-point probe (4-pp), TDTR, and SSTR techniques. We derived the electrical thermal conductivity of Cu from the 4-pp measured electrical resistivity applying Wiedemann-Franz Law assuming the low temperature value of the Lorenz number (2.44×10^{-8} $W\Omega K^{-2}$). In general, the SSTR-measured in-plane thermal conductivity of as-depsoited and annealed thin Cu films complies with these electrical-resisivity derived thermal conductvities within the uncertainty.

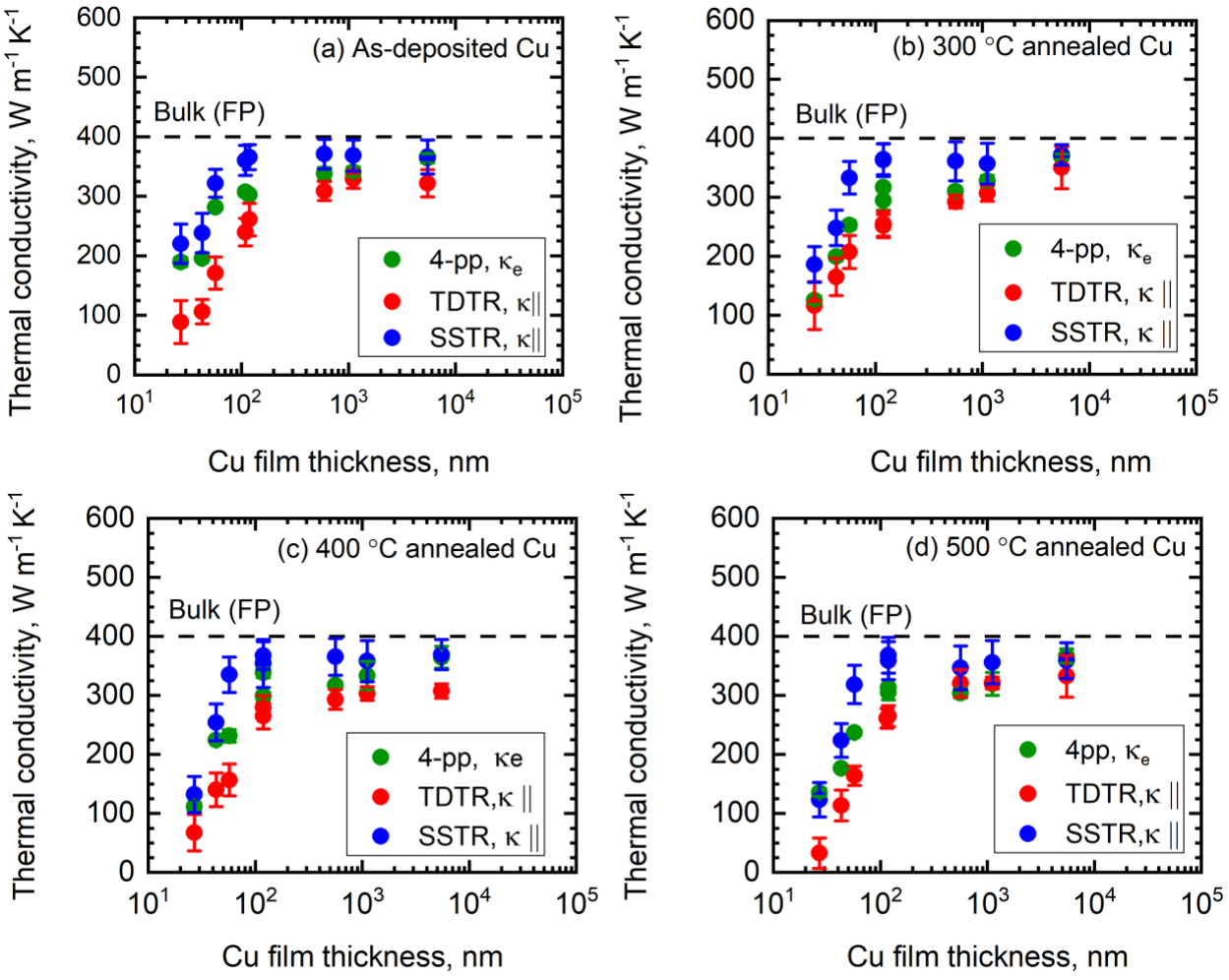

Figure S26: (a), (b), (c) and (d) comparison of 4-point probe, TDTR and SSTR measured in-plane thermal conductivity of as-deposited and annealed Cu films. The dashed line represents the calculated bulk thermal conductivity of Cu from our first-principles (FP) calculations

However, the TDTR measured in-plane thermal conductivities of thin Cu films (thickness< 500 nm) are lower than that of 4-pp and SSTR measured ones. TDTR underpredicts this thermal conductivity of thin Cu films because of its high sensitivity to various interface resistances of thin film stacks compared to the SSTR one as shown in Figure S27(a), (b), (d) and (e). TDTR includes the resistances from the interfaces of the film stacks that we cannot separate during analysis leading to a lower thermal conductivity[32] .Hence, TDTR measured thermal conductivities of 27, 44, 57, 118 nm films are generally lower than those measured with SSTR. The TDTR sensitivity to interface resistance reduces for thicker Cu film as shown in Figure S27(c) and (f), consistent with our measured values of TDTR agreeing with those determined by SSTR for these thicknesses. Therefore, the lower thermal conductivity of thin Cu films could be the artifact of TDTR measurements representing "effective" in-plane thermal conductivities of the Cu that include the effects of interfaces, where SSTR measurements report values that are more indictive of the intrinsic values.

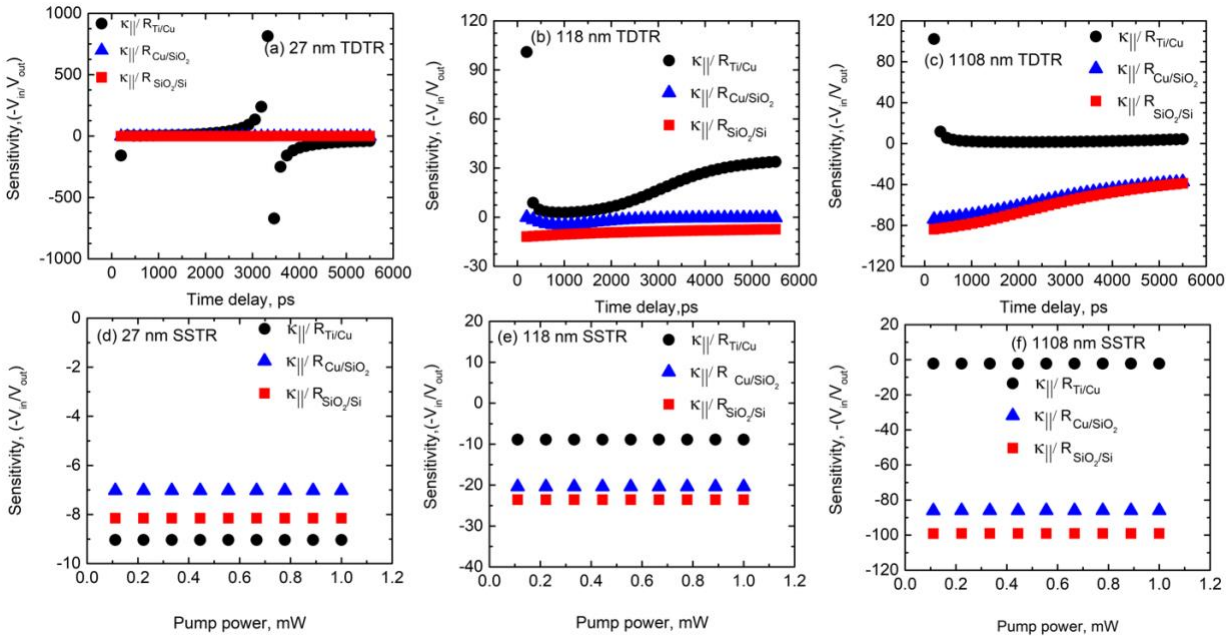

Figure S27: TDTR and SSTR sensitivities to the ratio of in-plane thermal conductivity and various interface resistances for 27 nm, 118 nm and 1108 nm films. (a) and (d) TDTR sensitivity to interface resistances of 27 nm film stacks is higher compared to SSTR. The TDTR sensitivity to interface resistance reduces with increasing thickness. (c) and (f) TDTR and SSTR sensitivities are comparable to various interface resistances of 1108 nm film stacks

The heat transport in the in-plane direction depends on the grain size of materials as found in several previous studies[33–35] We also observe a similar trend in our current study. Figure S28 shows the grain-size dependent in-plane thermal conductivity of as-deposited. We find that the SSTR measured in-plane thermal conductivity of as-deposited Cu films (thickness > 100 nm) within the uncertainty is close to our calculated bulk value, and consistent with the literature[36] as depicted in Figure S26. At these thicknesses, both the grain sizes and film thicknesses are larger than our calculated electronic mean free path ($\lambda_{ep} \approx 39$ nm) as shown in Figure S28. The reduction in

thermal conductivity for as-deposited 43 nm and 57 nm films from the bulk value is due to its grain size being smaller or close to the electron mean free path even though the film boundary is larger than the electron mean free path. For 27nm film both the grain size and thickness are less than the electron mean free path.

With the Sommerfeld value as a reference, the SSTR and 4-pp thermal conductivity measurements typically align and exhibit similar trends within the bounds of our experimental uncertainty. This convergence is primarily due to the minimal contribution of phonons to the thermal conductivity of Cu (<6% for the bulk value) [37,38]. The slight variance observed in films can be attributed to electron-grain boundary scattering, as depicted in Figure S28. In contrast to the SSTR, the thermal conductivity measured by 4-pp demonstrates greater sensitivity to electron-grain boundary scattering. Previous research has shown that grain boundary scattering affects electrical conductivity more than in-plane thermal conductivity[39–41], resulting in a higher Lorenz number than the reference value, L_0. As previously mentioned, the grain size of these films is either smaller than or approaches the length scale of the electron mean free path, causing the 4-pp measured thermal conductivity to deviate from that measured by SSTR.

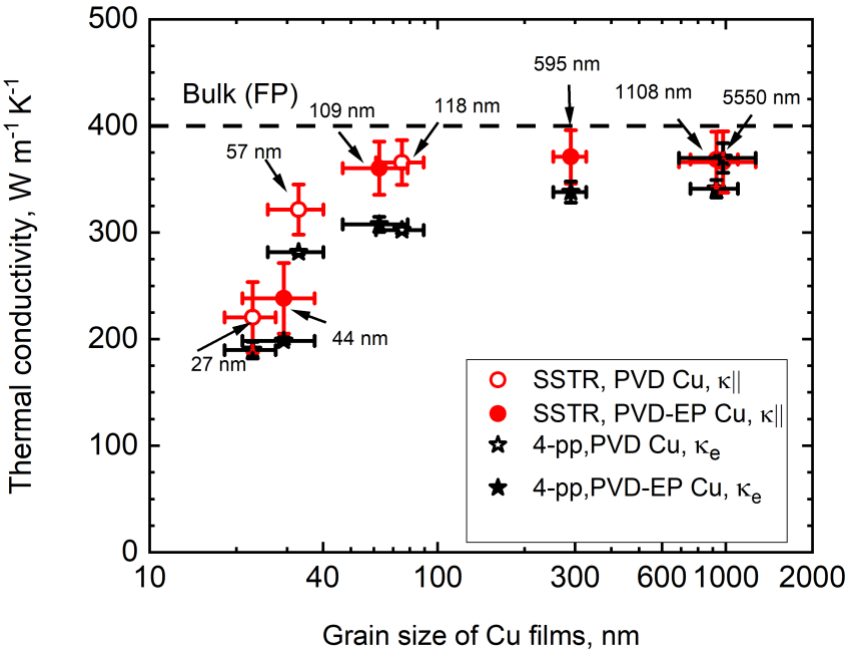

Figure S28: SSTR measured in-plane thermal conductivity and the calculated electron thermal conductivity from Wiedemann-Franz law using Sommerfeld value (L_0 = 2.44×10-8 WΩK^{-2}) of Cu films as a function of their grain size. The thickness of the films is also indicated with arrows. *The dashed line represents the calculated bulk thermal conductivity of Cu from our first principles (FP) calculations.*

S6. Details on two temperature model (TTM) and electron-phonon coupling factor determination.

We further study the electron scattering mechanisms in Cu films employing an ultrafast (sub-picosecond) pump-probe technique with wavelength tunability into the infrared to monitor the intraband transient thermoreflectance response of the Cu films. In this experiment, we pump the electrons in Cu films out of the equilibrium with the phonons at 2.38 eV energy. Then we probe the thermoreflectivity of the heated Cu films as a function of pump-probe delay time with a probing energy of 0.775 eV. This probing energy is far from the interband transition energy of Cu (2.16 eV) [42,43] and allows us to measure nearly free electron like reflectivity response. Probing the free-electron dynamics after pump heating simplifies the extraction of the electron–phonon coupling factor (*G*) from transient optical response of the films[44]. This is because the thermoreflectivity response is linearly proportional to the temperature of the phonon sub-system at probing energies far from the interband transition threshold[45,46] . The thermoreflectance contributions from the electron subsystem, which depends strongly on interband transitions, becomes negligible at energies far from these transitions. We perform the measurements at low pump power to avoid electron temperature dependent nonlinearity in thermophysical properties[9]. The incident pump fluence is set at ≈ 9.94 J m^{-2} for all films which induces a maximum electron perturbation temperature of ΔT_e =1132.23 K and maintain liner relationship between the electron temperature and thermophysical properties. Figure S29 shows the thermoreflectance of as-deposited PVD-EP Cu films. The free electrons transfer their energy to the phonons via electron-phonon scattering in less than a picosecond. The rise time for the reflectance signals of the as-deposited film thickness ranging between 44 nm and 5 μm does not show a thickness-dependence, indicating that electron transferring energy to phonons does not depend on film thickness and grain size. We observe similar thermoreflectance behavior from annealed films.

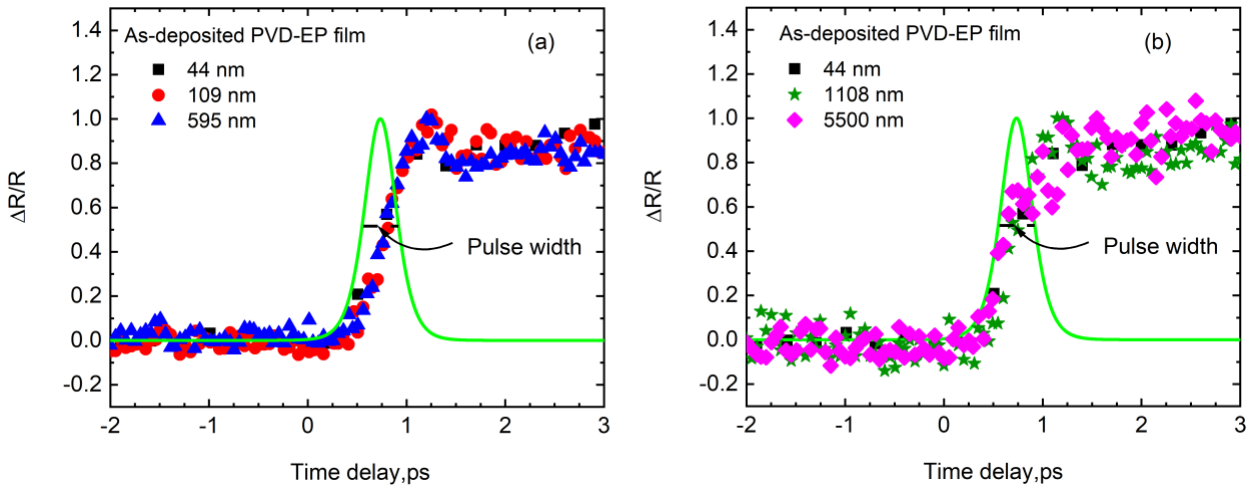

Figure S29: Normalized thermoreflectance as a function of pump-probe delay time for as-deposited 44, 109, 630, 1108 and 5500 nm Cu films at probing energy of 0.775 eV. Pulse duration of the pump is found to be 379 fs measured by fitting the thermoreflectance signals of Pt using sech^2 time function.

We employ the following two-temperature model (TTM) to extract the electron-phonon coupling factors of the Cu films:

$$C_e(T_e)\frac{\partial T_e}{\partial t} = \nabla \cdot (\kappa_e \nabla T_e) - G(T_e - T_p) + S(x,t) \qquad (S10)$$

$$C_p(T_p)\frac{\partial T_p}{\partial t} = \nabla \cdot (\kappa_p \nabla T_p) + G(T_e - T_p) \qquad (S11)$$

where C_e and C_p are the heat capacities of the electrons and phonons, respectively, and T_e and T_p are the temperatures of the electrons and phonons, respectively. S (x, t) which is the source term can be expressed by the following equation[47] :

$$S(x,t) = (1 - R_{opt})\frac{1.76J}{2t_p} \cdot sech^2\left[\left(\frac{1.76(t_o - t)}{t_p}\right)\right]\frac{dI}{dx} \qquad (S12)$$

In this equation, R_{opt} represents the surface reflectivity, *J* is the incident fluence, t_p represents pulse width of the pump pulse, $\frac{dI}{dx}$ is the light intensity profile determined via a transfer matrix method with optical constants at the pump wavelength of 520 nm. Here, we calculate the light intensity profile according to the Beer–Lambert law and a sech^2 pulse shape in the time domain.

To calculate the electron-phonon coupling factor, we solve the coupled differential equations in the TTM using a Crank-Nicolson method[48]. The discretization dimensions in time (dt= 50 × 10^{-15} s) and space (dx= 0.5 ×10^{-9} m) are chosen to ensure numerical stability for given material parameters listed in Table S5. To model energy deposition into the electronic system via the source term *S*, we utilize a transfer matrix method to determine the intensity of the light distribution in this Cu/100nm SiO_2/Si system[49] . We consider 3 nm Ta as an interface between Cu and 100 nm SiO_2. The thermal conductivity terms of TTM model (equations S10 and S11) are neglected to calculate *G* of the 27 nm film since this thin film is homogeneously heated at timescales corresponding to electron–phonon coupling. The electron mean free path is larger than 27 nm and the optical skin-depth of the pump beam is ~15 nm[50] . We consider the thermal conductivity terms of TTM for all other films (thickness: of 43 nm - 5 μm) to calculate their G. The similar approach is adopted for as-deposited and annealed films as discussed in the following section. We also assume that the electronic heat capacity varies linearly with electron temperature and electron - phonon coupling factor is constant with the temperature.

We calculate the lattice and electron temperature from the various thermophysical properties listed in Table S5 using TTM simulation. Since our probing energy is far from interband transition energies, we convert the TTM simulation into the optical response by calculating the normalized lattice temperature and comparing it to the normalized reflectivity from our thermoreflectance measurements using this model, where we normalize our data to the average value of ΔR/R between 1 – 3 ps. We then fit for *G* in the range of 0 to 2 ps. We choose this time regime as it should allow sufficient time for the electrons to couple to phonons and for maximum lattice temperature to be reached[42,43,51] (Figure S30).

Table S5: Parameters utilized for the two-temperature model calculations in this work. Here β is the temperature-dependent coefficient of the electronic heat capacity ($C_e = \beta T_e$), C_p is the phonon heat capacity, and κ_e and κ_p are the thermal conductivity of the electron and phonon subsystems, respectively. κ_e of Cu and Pt is determined from 4-pp measurements on our films. Electronic thermal boundary resistance is negligible and phononic thermal boundary resistance between Cu/SiO_2= 5 m^2 K GW^{-1} [24] ,Pt/SiO_2=5 m^2 K GW^{-1} [24], SiO_2/Si=4.35 m^2 K GW^{-1} [23,24]

Parameters	Cu	Pt	SiO_2	Si
Electron heat capacity coefficient, β (J m^{-3} K^{-2})	96.8 [9]	748.1[9]	0	0
Electron thermal conductivity, κ_e (W m^{-1} k^{-1})	120-400	40	0	0
Phonon thermal conductivity, κ_p (W m^{-1} k^{-1})	5-20 [37,38]	4[52,53]	1.35 [1,22,24,25]	130 [22,24]
Phonon heat capacity, C_p (MJ $m^{-3}K^{-1}$)	3.42	2.62	1.62[22–24]	1.65[1,22–25]

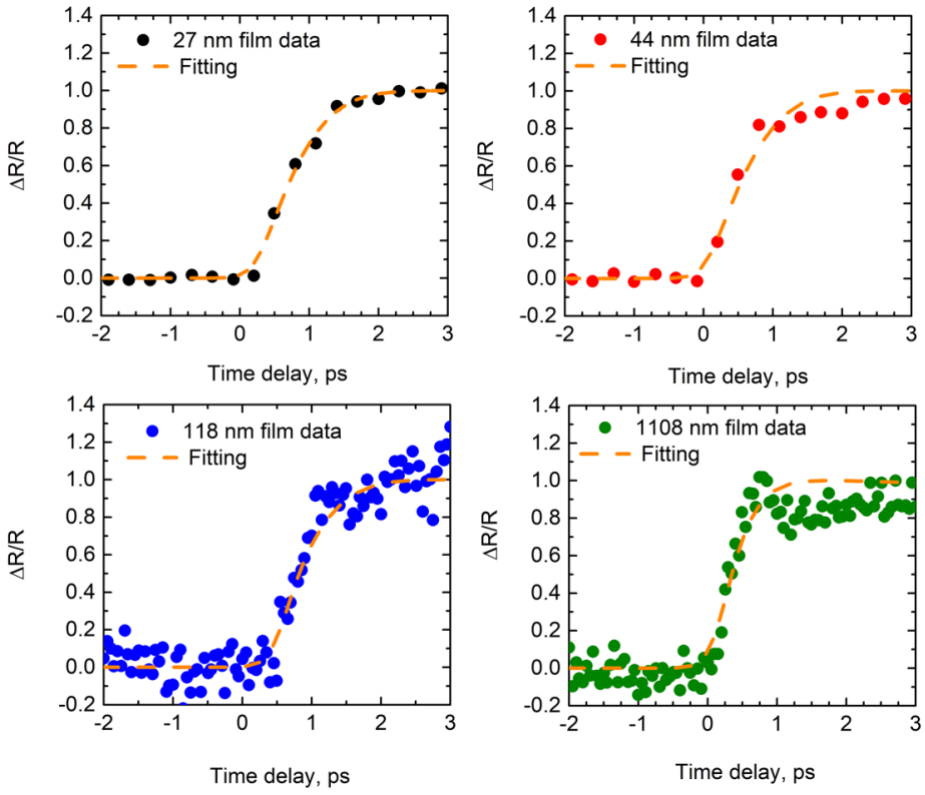

Figure S30: Experimental data for as-deposited 27, 44, 118, and 1108 nm Cu films at probing energy of 0.775 eV. The orange dashed line is the best fit to experimental data.

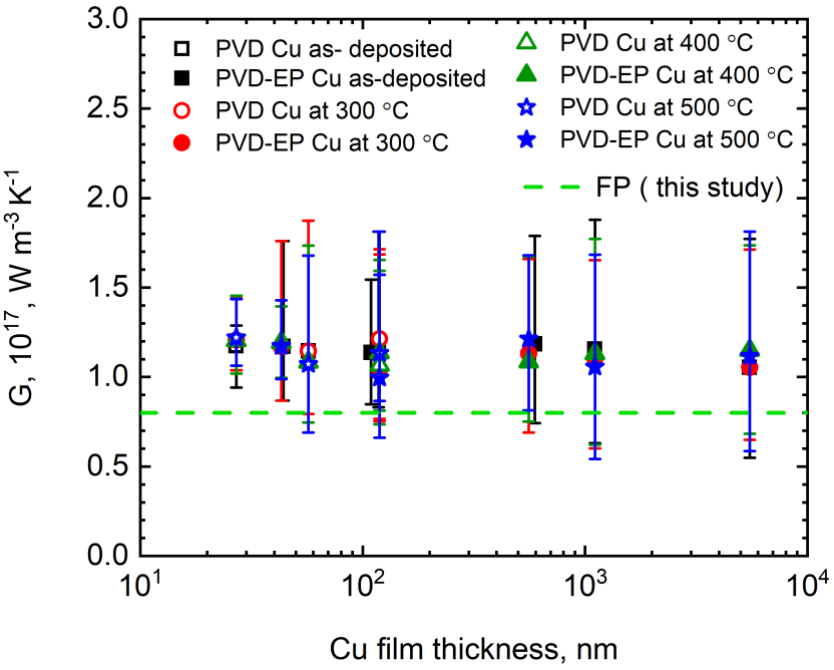

Figure S31: Two temperature model-derived G of the as-deposited and annealed film. G is constant with film thicknesses within uncertainty. Our TTM-derived G is in agreement with our first principles calculations (dashed line)

Applying the aforementioned methods, we obtain *G* of the as-deposited and annealed films from TTM. Figure S31 displays TTM derived *G* of as-deposited and annealed Cu films ranging from $1.06 \times 10^{17} - 1.18 \times 10^{17}$ $Wm^{-3}K^{-1}$. *G* of the Cu films is relatively constant for as-deposited and annealed Cu film regardless of the thickness and grain size. While performing this analysis we verify if the fitting parameters of TTM have sufficient sensitivity in determining *G* accurately. Although the characteristic shape of a 0-2 ps time regime is mostly due to electron-phonon coupling, there exists a range of electron-phonon coupling values for Cu in our measurements due to the noise in the experimental data resulting in multiple acceptable fits to experimental data. Having a wide range of electron-phonon coupling factors, we determine the uncertainty by using a type of contour plot that characterizes the similarity of various fits between the experiment and model. We generate the optical response curve using TTM for a given best-fit set of material properties (Table S5) and then perturb *G* by re-fitting. Here we only fit for the time at which the pulse hits the sample (an arbitrary parameter in our TTM). How close this modified curve is to the experimental data, in comparison to the best-fit curve, determines the uncertainty bounds on our analysis. In quantifying this we utilize an equation following Feser et al. [26]:

$$Z(G) \equiv \left(\frac{\sum[reflectivity(t;G_{exact}) - reflectivity(t;G_{perturbed})]^2}{\sum reflectivity(t;G_{exact})^2}\right)^{\frac{1}{2}} \quad \text{(S13)}$$

The contour of Z(G) represents the fits that are similar and dissimilar to one another in the least-squared sense where the curvature on each side of best-fit value (minimum value) determines the uncertainty. Depending on our data quality we choose 0.5% residual threshold within which the TTM model generates the same quality of fit to the experimental data as shown in Figure S32. We

include this 0.5% residual uncertainty to the uncertainty in our G calculations. We also notice that lower and upper bounds of error bar is asymmetric. The contour stretches towards higher G values from the best fit values as the thickness of the films increases. Looking at the contour on either side of the best-fit, the maximum *G* value can be measured with our TTM simulation is ~4.0x10^{17} $Wm^{-3}K^{-1}$.

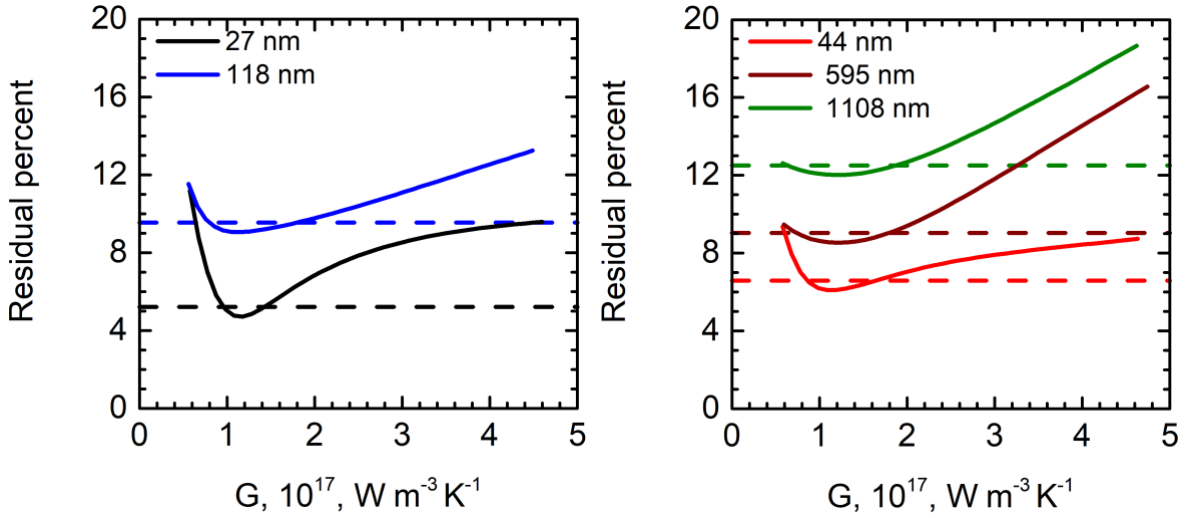

Figure S32: 2D contour analysis of G for as-deposited Cu films assuming the quality of fit based on the TTM model parameters and experimental data is within 0.5% threshold value.

S07. Pulse width determination for ultra-fast pump probe technique

We determine the pulse width of the pump pulse by measuring the thermoreflectance of 50 nm Pt/100 nmSiO_2/Si. The relatively high electron-phonon coupling factor of Pt is found not to be sensitive to the pulse width of pump. For an electron temperature rise of 100-500 K, *G* of Pt varies between 2-10× 10^{17} W $m^{-3}K^{-19}$. To measure the pulse width, we excite the electrons of Pt film out of their equilibrium at a pumping pulse of 2.38 eV and then probe the thermoreflectivity of the heated Pt films at an energy of 0.775 eV. We set the incident pump fluence at $\approx$ 5.9 J m^{-2} which leads to a maximum electron temperature rise of ΔT_e = 326 K. Figure S33 depicts the normalized thermoreflectance signal of Pt as a function of pump-probe delay time. We fit this curve for the pulse width with TTM simulation and the pulse width of pump is found to be 379 fs. The parameters used for the modeling are listed in the Table S5.

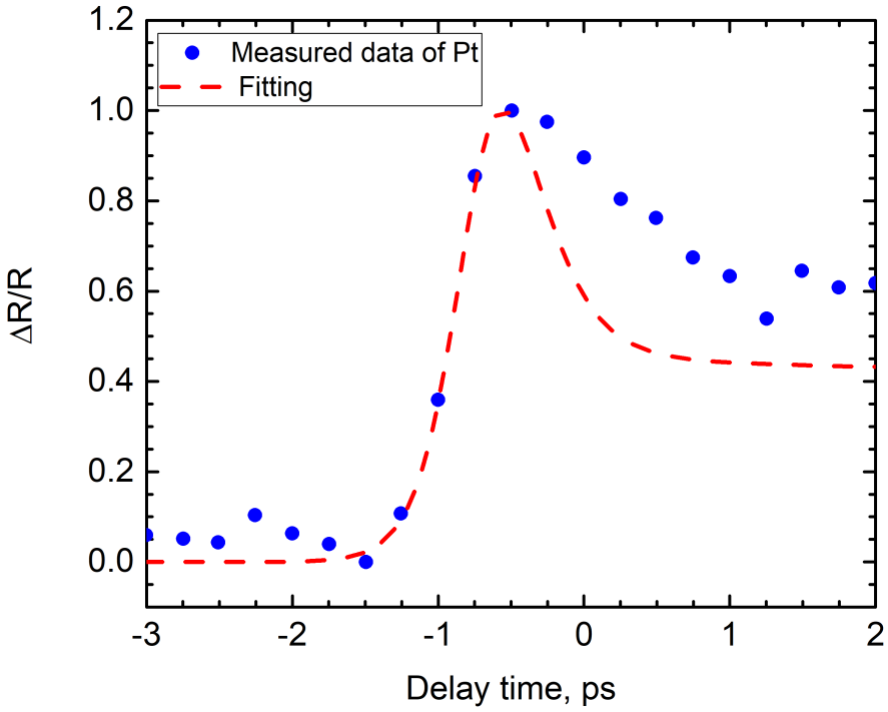

Figure S33: Normalized thermoreflectance as a function of pump-probe delay time for 50 nm Pt films at a probing energy of 0.775 eV. The Pulse duration of the pump is found to be 379 fs measured from the fitting of thermoreflectance signals.

S08. Effect of excitation energy, probing energy and pulse width on the electron-phonon coupling factor determination

Our calculated electron-phonon factor is insensitive to the changes to the pump and probe energies and laser pulse duration[54]. Longer pulse durations and lower perturbation energy can minimize the contribution of non-thermalized electrons to the electron-phonon coupling factor, leading to a more consistent coupling factor[9,55]. In our current pump-probe spectroscopy experiments, the pulse width is 379 fs, which exceeds the total electron thermalization time of Cu[56–58]. Therefore, at these timescales in which we determine G, we do not expect a long-lived non-thermal distribution rather, the electron system is expected to have a near-thermalized thermalized Fermi distribution. Importantly, the incident pump fluence is set at ≈ 9.94 J m^{-2} for all our Cu films, inducing a maximum electron perturbation temperature of ΔT_e =1132.23 K, maintaining a liner relationship between the electron temperature and thermophysical properties (electron heat capacity and electron coupling factor).[9] This electron perturbation temperature is too low (< 3000K) to induce significant electron-electron scattering [54,59] process and thus does not affect the electron-phonon scattering rate. Consequently, we measure the response of a near-thermalized Fermi distribution of electrons that cool solely due to electron-phonon scattering. This process is indicative of the scattering that influences the electron thermal conductivity of Cu[10].

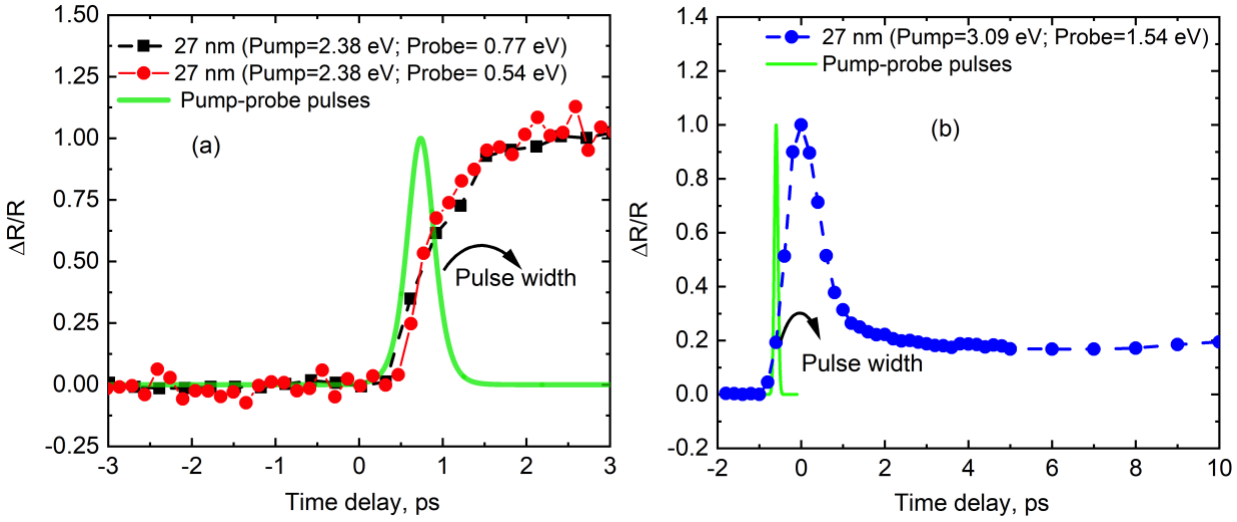

Figure S34: Normalized thermoreflectance as a function of pump-probe delay time for as-deposited 27 nm Cu films (a) Here the pump energy is set at 2.38 eV. Probing energies are 0.77 (ΔT_e =1132.23 K) and 0.54 eV (ΔT_e =1097.37 K) respectfully. Pulse duration of the pump is ~379 fs (b) The pump is at 3.09 eV and probe is at 1.54 eV. The maximum electron perturbation temperature is *~1000 K*

To substantiate the argument presented, we adjust both the pump and probe energies while maintaining the *maximum electron* perturbation temperature at ~ 1132 K, and find that the electron-phonon coupling factor remains consistent. Figure S34a displays the thermoreflectance of a 27 nm PVD Cu film with probing energies of 0.77 eV and 0.54 eV. The data indicate that free electrons transfer their energy to phonons through electron-phonon scattering in less than a picosecond. Notably, the rise time of the reflectance signals is unaffected by the probe energy. Additionally, we evaluated the thermoreflectance responses of 57 nm, 118 nm PVD, and 44 nm PVD-EP films at a probe energy of 0.54 eV. Figure S37 confirms that the coupling factors obtained using the two-temperature model (TTM) for these films are in good agreement with those derived from our measurements at 0.77 eV probing energy.

We utilize another pump-probe spectroscopy (pulse width ~100 fs) and increase the pump photon energy to 3.09 eV and probe energy to 1.54 eV. The details of this experimental set-up is explained in our previous works.[60,61] Briefly, we use a frequency modulated pump beam (3.09 eV) to irradiate the sample while the change in reflectivity is measured using a time delayed probe beam (1.54 eV). The pump and probe beams are focused onto the sample using an objective of 10X magnification with $1/e^2$ radii of the pump and probe spots being ~6 μm. At this higher probe energy, which exceeds the interband transition energy of Cu, the thermoreflectance signal is significantly affected by interband contributions, resulting in a marked reduction in the modulated response (Figure S34b). The coupling factor is calculated using the TTM (equation S10 and S11), where reflectivity changes are translated into temperature variations by incorporating electron-electron and electron-phonon collision rates. The laser source term S(t) for this pump-probe spectroscopy is calculated as follows:

$$S(t) = \frac{0.94F(1-R)}{d(t_p+t_{ee})} \exp\left(\frac{-2x^2}{r_0^2}\right) \exp\left\{-2.77\left[\frac{t-2(t_p+t_{ee})}{t_p+t_{ee}}\right]^2\right\} \quad \text{(S14)}$$

F represents the fluence of the laser incident on the surface of the sample, *R* is the reflectivity of the sample, r_0 denotes the radius of the laser spot, *d* is the film thickness, t_p is the width of the laser pulse, and t_{ee} is the electron-electron thermalization time, which is the time required for electrons to relax to a Fermi distribution following pulse absorption.[60] The parameters used in these calculations are same as our previous work.[61]

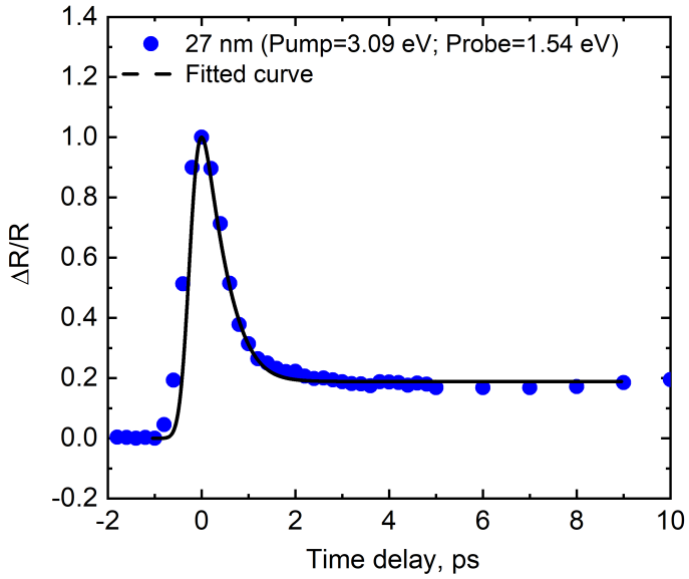

Figure S36: Measurement of electron-phonon coupling for 27 nm thick copper film using pump-prob spectroscopy. The blue circles indicate our experimental data while the black dashed line indicates the fitting obtained from the TTM.

In the case of thin films with electron mean free path larger than the thickness of the thin films, electrons travel ballistically and scatter at the boundaries. There is no diffusive scattering, and the TTM can be further simplified as follows:[63]

$$C_e(T_e)\frac{dT_e}{dt} = -G\left(T_e - T_p\right) + S(t) \quad \text{(S15)}$$

$$C_p\left(T_p\right)\frac{dT_p}{dt} = G\left(T_e - T_p\right) \quad \text{(S16)}$$

With:

$$\nabla \cdot (k_e \nabla T_e) = 0$$
$$\nabla \cdot \left(k_p \nabla T_p\right) = 0$$

the change in reflectivity was converted into a change in temperature by implementing electron-electron and electron-phonon collisional frequencies. In the case of metals, these frequencies depend on the temperature, as demonstrated by the following relations:

$$\nu_{ee} = A_{ee}T_e^2 \quad \text{(S17)}$$

$$\nu_{ep} = B_{ep}T_p \quad \text{(S18)}$$

With A_{ee} and B_{ep} being scattering coefficients calculated from the transient measurements. The scattering coefficients A_{ee} and B_{ep} are calculated starting from the following equation[64]:

$$G = \frac{\pi^2 m_e v_s^2 n_e}{6}\left[A_{ee}\left(T_e + T_p\right) + B_{ep}\right] \quad \text{(S19)}$$

m_e is the free electron mass, v_s is the Debye speed of sound, and n_e is the free electron number density. Using these equations, we obtain a G $=1.1\times 10^{17}$ W m^{-3} K^{-1} with $A_{ee}= 1.2 \times 10^{7}$ and $B_{ep}=1\times 10^{11}$ for 27 nm thick Cu film. Note G is not affected by electron-electron or electron-interface scattering[9].The measured G also matches closely with our infrared measurements.

The coupling factor derived from the thermoreflectance data, dominated by interband transitions, is consistent with that obtained from intraband transitions (Figure S37). Despite the increased excitation energy and the use of a ~100 fs pulse width to capture non-thermal distributions, the very low perturbation energy results in minimal contribution from electron-electron interactions to the electron-phonon coupling factor. This finding supports the importance of perturbation energy in modulating the electron-phonon coupling. Therefore, we conclude that the coupling factor is constant across various pump-probe energies within the Brillouin zone, due to the lower perturbation energy and longer pulse durations. Our pump-probe spectroscopy measurements represent the behavior of electrons within a few k_BT of the Fermi level, which contribute to the thermal transport properties of Cu.

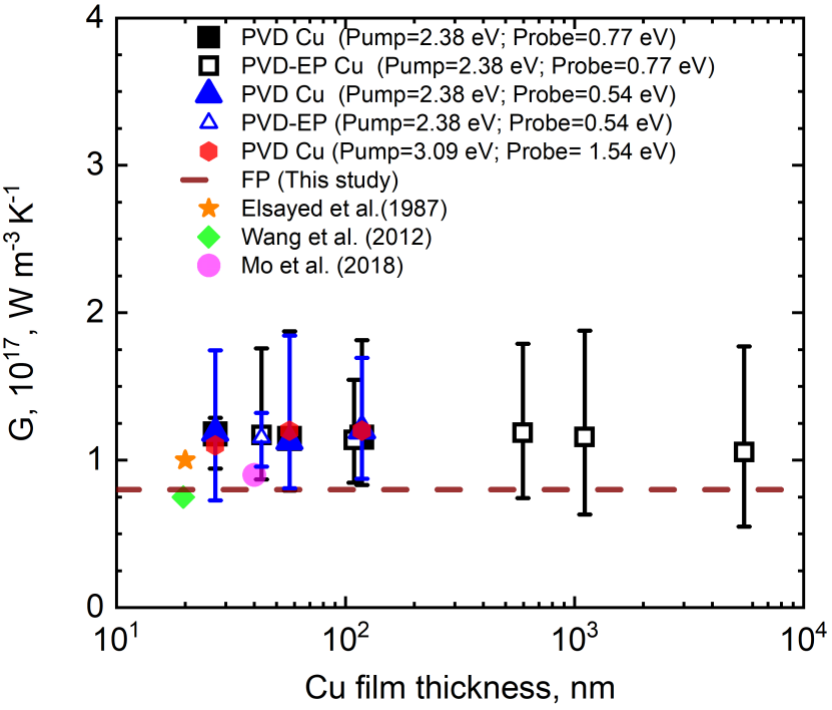

Figure S37: Two temperature model derived electron–phonon coupling factor (G) of the as-deposited films. The black square symbols represent the G of films measured at 0.77 eV probing energy. The blue triangle symbol exhibits the measurements taken at 0.54 eV probing energy. The red hexagonal symbol shows the data of probing energy= 1.54 eV and pump energy= 3.09 eV.

S09. Effective electron relaxation time determination with an infrared ellipsometer

We find the effective electron relaxation time in the Cu films from fitted oscillator models on complex frequency-dependent ellipsometric data. The ellipsometry measurements acquire the change in polarization of the light reflected from the sample in terms of amplitude ratio (Ψ) and phase difference (Δ). These ellipsometric values are related to the complex reflection coefficients (r_p and r_s) of the sample for *p*- and *s*-polarized light as:

$$\rho = \frac{r_p}{r_s} = \tan\Psi\, e^{i\Delta}$$

We obtain the ellipsometric data in the spectral range of 750-5000 cm^{-1} (2-13.33 μm) using an infrared ellipsometer (IR-VASE Mark II, J.A. Woollam Company). We perform the measurements at two incident angles of 60° and 70°, with a resolution of 16 cm^{-1} (~2 meV). Figure S38a shows the measured data for as-deposited Cu films with thicknesses ranging from 27 nm to 1108 nm.

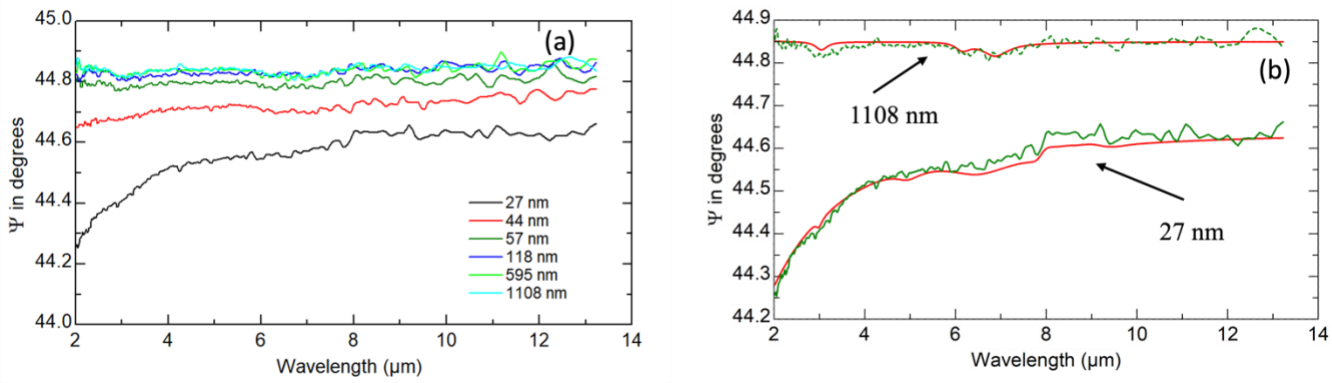

Figure S38: (a) Measured ellipsometry data at the incidence angle of 60° for as-deposited Cu films with various thicknesses. (b) Comparison of measured ellipsometry data (green lines) for 27 nm and 1108 nm Cu films with modeling results (red lines) fitted on the measured data.

We create an isotropic multi-layer optical model on this measured ellipsometric data to extract the complex frequency-dependent dielectric function of the Cu film. The literature values were used for the dielectric functions of the silicon substrate and thermal SiO_2 layer[65] . The free-electron contribution dominates the optical properties of the Cu films in the infrared regime. As such, we utilize the Drude free-electron model to determine the optical properties of these films as[66] :

$$\varepsilon_{Drude}(\omega) = \varepsilon_1(\omega) + i\varepsilon_2(\omega) = 1 - \frac{\omega_p^2}{\omega^2 + i\Gamma\omega}$$

where ω_p and Γ are the plasma frequency and the scattering rate, respectively. We optimize the parameters of the Drude model by minimizing the mean square error so that the modeled and measured ellipsometric data agree. Figure S38b shows the comparison between modeling results fitted on the measured data for two representative as-deposited Cu films (with thicknesses of 27 nm and 1108 nm) at the incidence angle of 60°. The mean squared errors for the fits performed on various thicknesses are below 0.3. Finally, we find the effective relaxation time of electron (τ) from the fitted scattering rate in the Drude model as $\tau = \Gamma^{-1}$.

The extracted effective relaxation time shows a thickness dependence as discussed in manuscript. This relaxation time is comparable with the effective thermal conductivity. We determine the effective thermal conductivity from the cross-plane and in-plane thermal conductivity as [22]:

$$\kappa_{effective,Cu} = \sqrt{\kappa_{cross-plane,Cu} \times \kappa_{in-plane,Cu}}$$

Figure S26a shows the SSTR measured the in-plane thermal conductivity and Figure S21 depicts the cross-plane thermal conductivity using TDTR. Even though the in-plane thermal conductivity remains almost constant for the as-deposited film thickness ranging between 100 and 1000 nm film thickness, the cross-plane thermal conductivity shows a thickness dependent trend since it is affected by the boundary scattering[67–69] . Because of this drop in cross-plane thermal conductivity, the effective thermal conductivity also shows a thickness dependence, even at a relatively large thickness of 100 nm as shown in manuscript. We observe that the effective thermal conductivity follows the same thickness dependent trend as the effective relaxation time of electron.

References

1. Cancellieri, C. *et al.* Interface and layer periodicity effects on the thermal conductivity of copper-based nanomultilayers with tungsten, tantalum, and tantalum nitride diffusion barriers. *Journal of Applied Physics* **128**, (2020).
2. King, S. W. *et al.* X-ray photoelectron spectroscopy measurement of the Schottky barrier at the SiC(N)/Cu interface. *Journal of Vacuum Science & Technology B, Nanotechnology and Microelectronics: Materials, Processing, Measurement, and Phenomena* **29**, (2011).
3. Giannozzi, P. *et al.* QUANTUM ESPRESSO: a modular and open-source software project for quantum simulations of materials. *Journal of Physics: Condensed Matter* **21**, 395502 (2009).
4. Poncï¿½, S., Margine, E. R., Verdi, C. & Giustino, F. EPW: Electron–phonon coupling, transport and superconducting properties using maximally localized Wannier functions. *Computer Physics Communications* **209**, 116–133 (2016).
5. Marzari, N., Mostofi, A. A., Yates, J. R., Souza, I. & Vanderbilt, D. Maximally localized Wannier functions: Theory and applications. *Reviews of Modern Physics* **84**, 1419–1475 (2012).
6. Troullier, N. & Martins, J. L. Efficient pseudopotentials for plane-wave calculations. *Physical Review B* **43**, 1993 (1991).
7. GRIMVALL, G. THE ELECTRON-PHONON INTERACTION IN METALS. *THE ELECTRON-PHONON INTERACTION IN METALS* (1981).
8. Gall, D. Electron mean free path in elemental metals. *Journal of Applied Physics* **119**, (2016).

9. Lin, Z., Zhigilei, L. V. & Celli, V. Electron-phonon coupling and electron heat capacity of metals under conditions of strong electron-phonon nonequilibrium. *Physical Review B - Condensed Matter and Materials Physics* **77**, 075133 (2008).
10. Giri, A., Tokina, M. V., Prezhdo, O. V. & Hopkins, P. E. Electron–phonon coupling and related transport properties of metals and intermetallic alloys from first principles. *Materials Today Physics* **12**, 100175 (2020).
11. Giri, A., Karna, P. & Hopkins, P. E. Exceptionally Enhanced Thermal Conductivity of Aluminum Driven by Extreme Pressures: A First-Principles Study. *Journal of Physical Chemistry Letters* **13**, 10918–10923 (2022).
12. Hopkins, P. E., Serrano, J. R., Phinney, L. M., Li, H. & Misra, A. Boundary scattering effects during electron thermalization in nanoporous gold. *Journal of Applied Physics* **109**, 13524 (2011).
13. Thomsen, C. *et al.* Coherent Phonon Generation and Detection by Picosecond Light Pulses. **53**,.
14. Thomsen, C., Maris, H. J. & Tauc, J. Picosecond acoustics as a non-destructive tool for the characterization of very thin films. *Thin Solid Films* **154**, 217–223 (1987).
15. Cahill, D. G., Goodson, K. & Majumdar, A. Thermometry and Thermal Transport in Micro/Nanoscale Solid-State Devices and Structures. *Journal of Heat Transfer* **124**, 223–241 (2002).
16. Hopkins, P. E. *et al.* Criteria for cross-plane dominated thermal transport in multilayer thin film systems during modulated laser heating. *Journal of Heat Transfer* **132**, 1–10 (2010).

17. Cahill, D. G. Analysis of heat flow in layered structures for time-domain thermoreflectance. *Review of Scientific Instruments* **75**, 5119–5122 (2004).
18. Wilson, R. B. & Cahill, D. G. Experimental Validation of the Interfacial Form of the Wiedemann-Franz Law. 255901–255902 (2012) doi:10.1103/PhysRevLett.108.255901.
19. Cheaito, R. *et al.* Thermal flux limited electron Kapitza conductance in copper-niobium multilayers. *Applied Physics Letters* **106**, 93114 (2015).
20. Gundrum, B. C., Cahill, D. G. & Averback, R. S. Thermal conductance of metal-metal interfaces. doi:10.1103/PhysRevB.72.245426.
21. Schmidt, A. J., Cheaito, R. & Chiesa, M. A frequency-domain thermoreflectance method for the characterization of thermal properties. *Review of Scientific Instruments* **80**, 94901 (2009).
22. Braun, J. L., Olson, D. H., Gaskins, J. T. & Hopkins, P. E. A steady-state thermoreflectance method to measure thermal conductivity. *Review of Scientific Instruments* **90**, 24905 (2019).
23. Braun, J. L. *et al.* Size effects on the thermal conductivity of amorphous silicon thin films. *Physical Review B* **93**, 140201 (2016).
24. Hoque, M. S. B. *et al.* Thermal conductivity measurements of sub-surface buried substrates by steady-state thermoreflectance. *Review of Scientific Instruments* **92**, 64906 (2021).
25. Scott, E. A. *et al.* Thermal resistance and heat capacity in hafnium zirconium oxide (Hf1-xZrxO2) dielectrics and ferroelectric thin films. *Applied Physics Letters* **113**, 192901 (2018).
26. Feser, J. P. & Cahill, D. G. Probing anisotropic heat transport using time-domain thermoreflectance with offset laser spots. *Review of Scientific Instruments* **83**, 104901 (2012).

27. Olson, D. H. *et al.* Band alignment and defects influence the electron-phonon heat transport mechanisms across metal interfaces. *Applied Physics Letters* **118**, 163503 (2021).
28. Wilson, R. B. & Cahill, D. G. Limits to Fourier theory in high thermal conductivity single crystals . *Appl. Phys. Lett* **107**, 203112 (2015).
29. Yang, J., Maragliano, C. & Schmidt, A. J. Thermal property microscopy with frequency domain thermoreflectance. *Review of Scientific Instruments* **84**, 104904 (2013).
30. Hoque, M. S. B. *et al.* High In-Plane Thermal Conductivity of Aluminum Nitride Thin Films. *ACS Nano* **15**, 9588–9599 (2021).
31. Pfeifer, T. W. *et al.* Measuring sub-surface spatially varying thermal conductivity of silicon implanted with krypton. *Journal of Applied Physics* **132**, (2022).
32. Zeng, T. & Chen, G. Phonon Heat Conduction in Thin Films: Impacts of Thermal Boundary Resistance and Internal Heat Generation. *Journal of Heat Transfer* **123**, 340–347 (2001).
33. Lee, D. *et al.* Dependence of the In-Plane Thermal Conductivity of Graphene on Grain Misorientation. *Chemistry of Materials* **29**, 10409–10417 (2017).
34. Anaya, J. *et al.* Control of the in-plane thermal conductivity of ultra-thin nanocrystalline diamond films through the grain and grain boundary properties. *Acta Materialia* **103**, 141–152 (2016).
35. Lee, W. *et al.* In-Plane Thermal Conductivity of Polycrystalline Chemical Vapor Deposition Graphene with Controlled Grain Sizes. *Nano Letters* **17**, 2361–2366 (2017).
36. Touloukian, Y. S., Powell, R. W., Ho, C. Y. & Klemens, P. G. *Thermal Conductivity: Metallic Elements and Alloy*. (1970).

37. Sæther, S. *et al.* Phonon thermal transport in copper: The effect of size, crystal orientation, and grain boundaries. *AIP Advances* **12**, 65301 (2022).
38. Stojanovic, N., Maithripala, D. H. S., Berg, J. M. & Holtz, M. Thermal conductivity in metallic nanostructures at high temperature: Electrons, phonons, and the Wiedemann-Franz law. *Physical Review B - Condensed Matter and Materials Physics* **82**, 075418 (2010).
39. Zhang, Q. G., Cao, B. Y., Zhang, X., Fujii, M. & Takahashi, K. Influence of grain boundary scattering on the electrical and thermal conductivities of polycrystalline gold nanofilms. *Phys. Rev. B* **74**, 134109 (2006).
40. Mayadas, A. F., Shatzkes, M. & Janak, J. F. ELECTRICAL RESISTIVITY MODEL FOR POLYCRYSTALLINE FILMS: THE CASE OF SPECULAR REFLECTION AT EXTERNAL SURFACES. *Applied Physics Letters* **14**, 345–347 (1969).
41. De Vries, J. W. C. Temperature and thickness dependence of the resistivity of thin polycrystalline aluminium, cobalt, nickel, palladium, silver and gold films. *Thin Solid Films* **167**, 25–32 (1988).
42. Elsayed-Ali, H. E., Norris, T. B., Pessot, M. A. & Mourou, G. A. PHYSICAL REVIEW LETTERS Time-Resolved Observation of Electron-Phonon Relaxation in Copper. **58**, (1987).
43. Eesley, G. L. Generation of nonequilibrium electron and lattice temperatures in copper by picosecond laser pulses. *Phys. Rev. B* **33**, 2144–2151 (1986).
44. Tomko, J. A., Kumar, S., Sundararaman, R. & Hopkins, P. E. Temperature dependent electron-phonon coupling of Au resolved via lattice dynamics measured with sub-picosecond infrared pulses. *Journal of Applied Physics* **129**, 193104 (2021).

45. Heilpern, T. *et al.* Determination of hot carrier energy distributions from inversion of ultrafast pump-probe reflectivity measurements. *Nature Communications 2018 9:1* **9**, 1–6 (2018).
46. Schoenlein, R. W., Lin, W. Z., Fujimoto, J. G. & Eesley, G. L. Femtosecond studies of nonequilibrium electronic processes in metals. *Physical Review Letters* **58**, 1680 (1987).
47. Sotrop, J., Kersch, A., Domke, M., Heise, G. & Huber, H. P. Numerical simulation of ultrafast expansion as the driving mechanism for confined laser ablation with ultra-short laser pulses. *Applied Physics A: Materials Science and Processing* **113**, 397–411 (2013).
48. Özışık, M. N., Colaco, M. J., Orlande, H. R. B. & Cotta, R. M. *Finite Difference Methods in Heat Transfer*. (Taylor & Francis, CRC Press, 2017).
49. Bhatia, A. B. *et al.* Principles of optics Electromagnetic theory of propagation, interference and diffraction of light with contributions by SEVENTH HEXPANDED) EDITION.
50. Johnson, P. B. & Christy, R. W. Optical Constants of the Noble Metals. *Physical Review B* **6**, 4370 (1972).
51. Wang, W. & Cahill, D. G. Limits to thermal transport in nanoscale metal bilayers due to weak electron-phonon coupling in Au and Cu. *Physical Review Letters* **109**, 175503 (2012).
52. Duggin, M. J. The thermal conductivities of aluminium and platinum. *Journal of Physics D: Applied Physics* **3**, L21 (1970).
53. Tong, Z., Li, S., Ruan, X. & Bao, H. Comprehensive first-principles analysis of phonon thermal conductivity and electron-phonon coupling in different metals. *Physical Review B* **100**, 144306 (2019).

54. Giri, A. & Hopkins, P. E. Transient thermal and nonthermal electron and phonon relaxation after short-pulsed laser heating of metals. *Journal of Applied Physics* **118**, 215101 (2015).
55. Allen, P. B. Theory of thermal relaxation of electrons in metals. *Phys. Rev. Lett.* **59**, 1460–1463 (1987).
56. Bigot, J.-Y., Merle, J.-Y., Cregut, O. & Daunois, A. Electron Dynamics in Copper Metallic Nanoparticles Probed with Femtosecond Optical Pulses. *Phys. Rev. Lett.* **75**, 4702–4705 (1995).
57. Bigot, J.-Y., Halté, V., Merle, J.-C. & Daunois, A. Electron dynamics in metallic nanoparticles. *Chemical Physics* **251**, 181–203 (2000).
58. Pogna, E. A. A. *et al.* Ultrafast Spectroscopy of Graphene-Protected Thin Copper Films. *ACS Photonics* **3**, 1508–1516 (2016).
59. Karna, P. & Giri, A. Electron–electron scattering limits thermal conductivity of metals under extremely high electron temperatures. *J. Phys.: Condens. Matter* **36**, 345701 (2024).
60. Karna, P., Hoque, M. S. B., Thakur, S., Hopkins, P. E. & Giri, A. Direct Measurement of Ballistic and Diffusive Electron Transport in Gold. *Nano Lett.* **23**, 491–496 (2023).
61. Karna, P., Islam, M. R., Hoglund, E. R., Hopkins, P. E. & Giri, A. Electron-phonon coupling dictates electron mean free paths and negative thermal diffusion in metals. *Materials Today Chemistry* **37**, 101991 (2024).
62. Elsayed-Ali, H. E., Norris, T. B., Pessot, M. A. & Mourou, G. A. Time-resolved observation of electron-phonon relaxation in copper. *Physical Review Letters* **58**, 1212 (1987).
63. Staechelin, Y. U., Hoeing, D., Schulz, F. & Lange, H. Size-Dependent Electron–Phonon Coupling in Monocrystalline Gold Nanoparticles. *ACS Photonics* **8**, 752–757 (2021).

64. Chen, J. K., Latham, W. P. & Beraun, J. E. The role of electron–phonon coupling in ultrafast laser heating. *Journal of Laser Applications* **17**, 63–68 (2005).

65. Herzinger, C. M., Johs, B., McGahan, W. A., Woollam, J. A. & Paulson, W. Ellipsometric determination of optical constants for silicon and thermally grown silicon dioxide via a multi-sample, multi-wavelength, multi-angle investigation. *Journal of Applied Physics* **83**, 3323–3336 (1998).

66. Fowles, G. R. *Introduction to Modern Optics*. (1989).

67. Gomes, C. J., Madrid, M., Goicochea, J. V. & Amon, C. H. In-Plane and Out-Of-Plane Thermal Conductivity of Silicon Thin Films Predicted by Molecular Dynamics. *Journal of Heat Transfer* **128**, 1114–1121 (2006).

68. Jeong, C., Datta, S. & Lundstrom, M. Thermal conductivity of bulk and thin-film silicon: A Landauer approach. *Journal of Applied Physics* **111**, 093708 (2012).

69. Kwon, S., Zheng, J., Wingert, M. C., Cui, S. & Chen, R. Unusually High and Anisotropic Thermal Conductivity in Amorphous Silicon Nanostructures. *ACS Nano* **11**, 2470–2476 (2017).